NASA Technical Paper 3000

June 1990

Dynamic Ground-Effect Measurements on the F-15 STOL and Maneuver Technology Demonstrator (S/MTD) Configuration

Guy T. Kemmerly

NASA

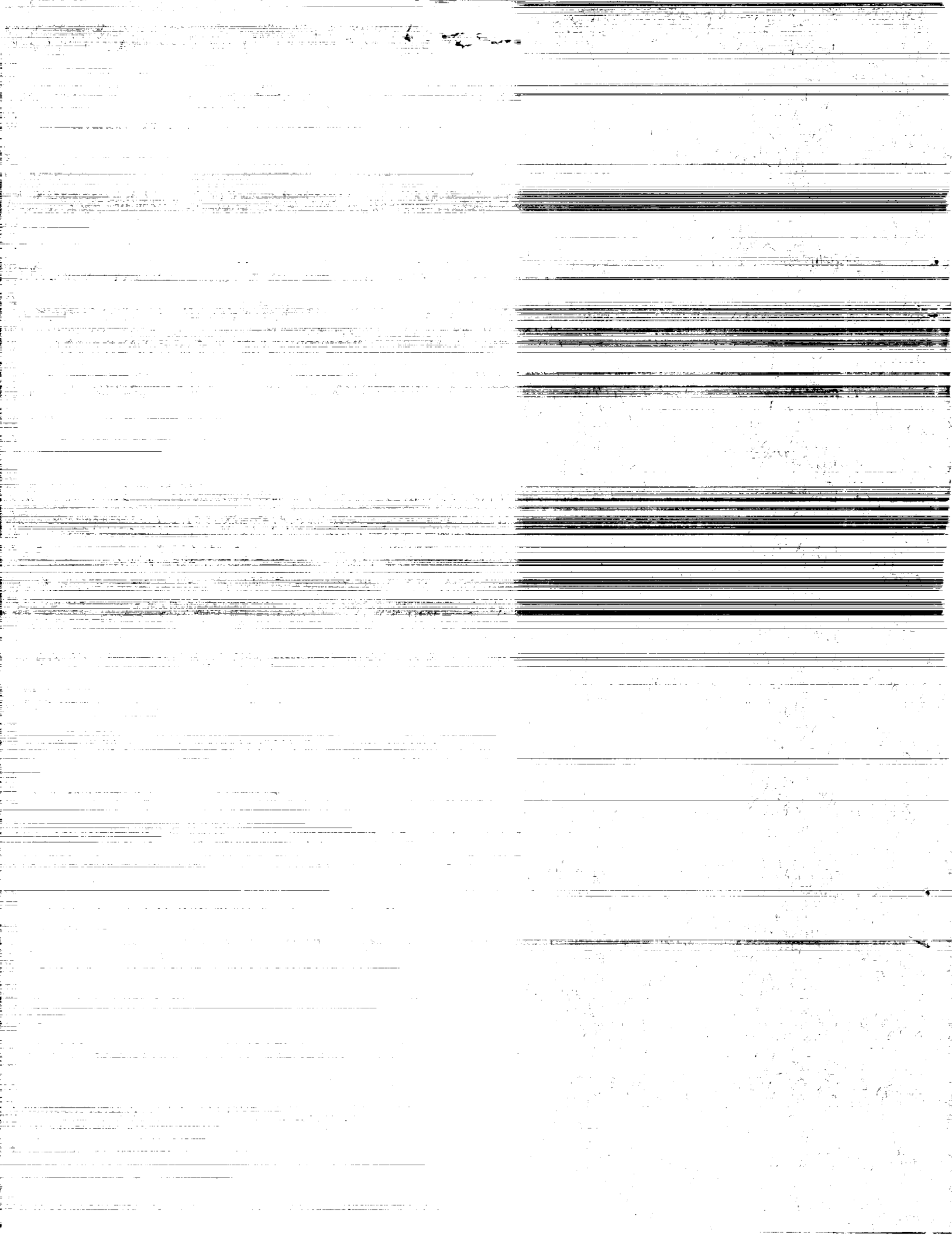

NASA Technical Paper 3000

1990

Dynamic Ground-Effect Measurements on the F-15 STOL and Maneuver Technology Demonstrator (S/MTD) Configuration

Guy T. Kemmerly
Langley Research Center
Hampton, Virginia

NASA
National Aeronautics and Space Administration
Office of Management
Scientific and Technical Information Division

Summary

A moving-model ground-effect testing method has been used to study the influence of rate of descent on the aerodynamic characteristics of the F-15 STOL and Maneuver Technology Demonstrator (S/MTD) configuration for both the approach and rollout phases of landing. The approach phase was modeled for three rates of descent and the results were compared with predictions from the F-15 S/MTD simulation data base (predictions based on data obtained in a wind tunnel with zero rate of descent). This comparison showed significant differences due both to the rate of descent in the moving-model test and to the presence of the ground boundary layer in the static wind-tunnel test. Relative to the simulation data base predictions, the moving-model test showed substantially less lift increase in ground effect, less nose-down pitching moment, and less increase in drag. These differences became more prominent at the larger thrust vector angles.

Over the small range of rates of descent tested using the moving-model technique, the effect of rate of descent on longitudinal aerodynamics was relatively constant.

The results of this investigation indicate no safety-of-flight problems with the lower jets vectored up to 80° on approach. The results also indicate that this configuration could employ a nozzle concept using lower reverser vector angles up to 110° on approach if a "no-flare" approach procedure were adopted and if inlet reingestion does not pose a problem.

Introduction

With the renewed interest in the tactical advantages of fighter/attack aircraft using short takeoff and landing (STOL) capabilities, aircraft designers are seriously considering the use of vectored/reversed thrust as a means of attaining short landings. However, the use of large thrust vectoring (including thrust reversing) in close proximity to the ground has been shown to strongly influence the flow field that forms beneath an aircraft in ground effect (refs. 1, 2, and 3). Furthermore, recent ground-effect studies at the Langley Research Center (LaRC) (ref. 4) conducted to explore the effect of rate of descent on aerodynamic ground effects have shown that the use of thrust vectoring and reversing significantly increases the influence of rate of descent on ground effects. These results have generated strong research interest in exploring the steady-state and dynamic ground effects on a configuration representative of the expected new generation of STOL fighters.

The F-15 STOL and Maneuver Technology Demonstrator (S/MTD) is a current representative of this new vehicle class incorporating vectored thrust. A description of this vehicle and the technology program surrounding it is presented in reference 5. This configuration was designed specifically to investigate and demonstrate the technologies for STOL fighters. It incorporates a three-surface design (canards, wings, and horizontal tails) and thrust vectoring and reversing capabilities to enhance STOL performance. Flight tests of this vehicle will provide a realistic assessment of the impact of vectored thrust on ground effects and may present the opportunity for comparing predictions with flight results at a later date. These flight results will be invaluable for assessing the proper methods needed to extrapolate (or scale) the subscale dynamic ground-effect measurements to full-scale applications. It was the purpose of the present investigation to define the subscale dynamic ground effects on the F-15 S/MTD configuration in preparation for a comparison with the flight-test data when they become available. A comparison of the dynamic measurements with the static wind-tunnel ground-effect measurements is also made.

Symbols

All moment data are referenced to the point located at $0.2526\bar{c}$ on the model. All results are presented in U.S. units. The coordinate systems used are illustrated in figure 1.

b	wing span, in
C_A	axial-force coefficient, Axial force/$\bar{q}S$
C_D	drag coefficient, Drag/$\bar{q}S$
ΔC_D	incremental drag coefficient, $C_{D,\text{instantaneous}} - C_{D,\infty}$
C_L	lift coefficient, Lift/$\bar{q}S$
ΔC_L	incremental lift coefficient, $C_{L,\text{instantaneous}} - C_{L,\infty}$
C_m	pitching-moment coefficient, Pitching moment/$\bar{q}S\bar{c}$
ΔC_m	incremental pitching-moment coefficient, $C_{m,\text{instantaneous}} - C_{m,\infty}$
$\bar{c}$	mean aerodynamic chord, 15.9 in.
g	Earth gravitational units ($1g \approx 32.17$ ft/sec^2)
h	height of model over ground board (referenced to $0.2526\bar{c}$), ft

$\dot{h}$	rate of descent, ft/sec
I_X	moment of inertia about X-axis, ft-lb-sec^2
I_Y	moment of inertia about Y-axis, ft-lb-sec^2
I_Z	moment of inertia about Z-axis, ft-lb-sec^2
$\dot{p}$	roll acceleration, radians/sec^2
$\dot{q}$	pitch acceleration, radians/sec^2
$\bar{q}$	dynamic pressure, lb/ft^2
$\dot{r}$	yaw acceleration, radians/sec^2
S	wing area, ft^2
V	velocity, ft/sec
X, Y, Z	body-axis system shown in figure 1
x	linear displacement along X-axis, ft
$\dot{x}$	linear velocity in x-direction, ft/sec
$\ddot{x}$	linear acceleration in x-direction, ft/sec^2
$\bar{x}, \bar{y}, \bar{z}$	distance from model center of gravity to balance moment center
y	linear displacement along Y-axis, ft
$\ddot{y}$	linear acceleration in y-direction, ft/sec^2
z	linear displacement along Z-axis, ft
$\ddot{z}$	linear acceleration in z-direction, ft/sec^2
α	angle of attack, deg
γ	flight path angle (incidence of model path relative to ground plane), deg
δ	deflection angle, deg
λ	frequency of periodic perturbation in configuration aerodynamics, Hz
ρ	density, slugs/ft^3

Subscripts:

a	aileron
B	base
c	canard
FF	flow field
FS	full scale
f	flap
h	horizontal stabilizer
j	jet
l	lower
M	model
osc	oscillatory
SS	steady state
u	upper
∞	free stream

Abbreviations:

AF	axial force
LaRC	Langley Research Center
NF	normal force
PM	pitching moment
psid	pounds per square inch referenced to atmospheric pressure
RM	rolling moment
SF	side force
S/MTD	STOL and Maneuver Technology Demonstrator
STOL	short takeoff and landing
VRF	Vortex Research Facility
YM	yawing moment

Facility

The Langley Vortex Research Facility (VRF) (illustrated in fig. 2) was used for the present study. In that facility the model is suspended on a variable-length strut extending from the bottom of the overhead gasoline-engine-powered cart. The strut supports the model and air line assembly as well as the instrumentation. The angle of attack was changed by pitching the entire strut and model assembly at the point where the strut was attached to the cart. Velocity was controlled by a cruise-control system on the cart. High-pressure air bottles on the cart provided compressed air for the thrust simulators.

For the present test, the test region of the VRF was modified to incorporate a 150-ft-long ground board near the center of the test section. The ground board consisted of two parts: a ramp inclined upward 4° for a distance of 100 ft, and a horizontal section following the ramp which extended for an additional 50 ft. The height of the model over the fixed horizontal portion of the ground board was set

by adjusting the length of the model support strut. As the model moved horizontally over the inclined portion, the distance from the ground board to the model reduced, thereby simulating an approach along a glide slope of 4°. The rate of descent was dependent on the test velocity as given by the equation

$$\dot{h} = V_\infty \tan 4°$$

After moving across the ramp, the model passed over the horizontal section to simulate rollout or constant-altitude flight. (See fig. 3.)

In the VRF 24 channels of digital data are transmitted from the cart through a modulated laser beam to a photo receptor and a mass data storage unit. The channels are sampled at a rate of 111 samples per second for nearly 30 sec. The data are then converted to engineering units using a Hewlett-Packard HP 1000 A900 computer. For more information on the data acquisition in the VRF, see reference 6.

Model

Three restrictions were placed on the investigation because of facility limitations. The first of these was a result of the width of the ground board installed in the facility. That ground board was constructed 8 ft wide. Using the VSAERO panel method described in reference 7 showed that the model span should be limited to approximately 3 ft to ensure that the boundaries of the ground board would not influence the ground effect on the configuration. For the S/MTD configuration this corresponds to an 0.08-scale model. The second facility restriction was that the model weight should be less than 80 lb because of cart support system limitations. Third, and finally, VRF testing is limited by maximum cart velocity to 100 ft/sec. An available 0.083-scale, low-speed, rotary-balance model of an F-15A aircraft was chosen based on these restrictions and was then modified to match the S/MTD configuration. This model configuration is shown in figures 4 and 5. Because that model was designed with a dynamic pressure limit ($\bar{q}$-limit) of 6 lb/ft^2, the upper limit of testing became 70 ft/sec. This model had adjustable tail surfaces, flaps, ailerons, and canards. The ranges of motion of these surfaces were sufficient to model properly the approach and rollout configurations of the S/MTD aircraft. The configurations tested are detailed in table I. Landing gear were not modeled in this investigation.

The model was mounted on a blade that entered the top of the model just behind the model reference point, 0.2526$\bar{c}$. The cross section of the blade was 5.5 in. long and 1 in. thick. The vectored thrust simulator was held in place in the cavity behind the model by two steel bars that attached to each side of the support blade approximately 15 in. above the model. The gaps between the vectored thrust simulator and the model and between the blade mount and the model were bridged by a thin rubber sheet (dental dam) to prevent flow inside the model. Because the distance was so small between the vectored thrust simulator and the model, an electrically charged copper strip (foul strip) was installed inside the cavity into which the thrust vector simulator fit. Monitoring the charge of the metal thrust vector simulator indicated when contact was made with the model.

Once mounted on the support strut in the VRF, it was noted that the model was slightly twisted along the X-axis. An attempt was made to level the model around that axis to minimize the impact of this model imperfection. The resulting roll deviations from horizontal of the three principal aerodynamic surfaces are detailed in table II. These small deviations were not expected to impact the results of the program.

To ensure that the flow on most of the model would be turbulent, 1/8-in-wide transition strips of No. 60 carborundum grit were placed on the model 1/2 in. back from the leading edges of the aerodynamic surfaces and 1 in. back from the nose.

Thrust simulation was supplied nonmetrically (thrust loads not measured by the balance) using the vectored thrust simulator described in reference 8 and sketched in figure 6. This device was attached to the sting and positioned (in the cutout in the model shown in fig. 4) such that the location of the nozzles corresponded to the location of the rotating-vane thrust reverser on the S/MTD. The jet was directed by honeycomb inserts embedded in the plenum box cover plate. Different plates directed the jet at different angles.

Instrumentation

Model forces and moments were measured with a six-component strain gauge balance (NASA LaRC balance VORTEX-5 with a 10-lb axial beam). Model accelerations necessary to remove the inertial loads from the balance outputs (see the appendix) were measured by Setra Systems $\pm 15g$ linear accelerometers calibrated over a range of $\pm 1g$. In the test section during the cruise portion of the runs, $\pm 1g$ was sufficient to encompass the accelerations of the vibrating model. The details of how these accelerations were used to remove the inertial loads from the balance data are given in the appendix.

In order to set the model jet conditions such that full-scale jet conditions would be modeled properly, jet-exit total-pressure measurements were necessary. These measurements were made statically and

were calibrated against total-pressure measurements taken in the plenum. Nozzle-exit pressures were measured using ±2-psid Endevco model 8510 pressure transducers, and plenum pressures were measured using ±10-psid CEC Model 4-312 pressure transducers. Jet total temperatures were measured with iron-constantan thermocouples located approximately 4 ft upstream of the plenum. Measurements not specific to this test such as vehicle velocity and atmospheric conditions at the time of the test were taken using the standard facility instrumentation, the details of which can be found in reference 6.

Scaling Considerations

Because the objective of this investigation was to model a dynamic event on a powered configuration, it was important that the jet conditions be matched to those at full scale and that the data be sampled and filtered such that information of interest to the full-scale aircraft be captured in the subscale testing.

Based on the results reported in reference 9, jet velocity was scaled using a ratio of dynamic pressures ($\bar{q}$-ratio) defined as $\bar{q}_j/\bar{q}_\infty$. The study reported in that reference considered several scaling parameters and found that the $\bar{q}$-ratio was most effective for correlating the data taken at different test conditions. For this investigation the condition tested was

$$\frac{\bar{q}_{j,M}}{\bar{q}_{\infty,M}} = \frac{\bar{q}_{j,\mathrm{FS}}}{\bar{q}_{\infty,\mathrm{FS}}} = 45$$

based on the expected flight conditions for the S/MTD. It is assumed that for the aircraft on approach, the engines will be set such that the exhaust nozzles will be choked. Therefore, it would have been desirable to test using choked flow in the vectored jets. However, to do so and match the full-scale $\bar{q}$-ratio of 45, a minimum test velocity of 166 ft/sec was required. Both the facility limitations and the model limitations made this impossible. With the model load limit as the determining factor, the maximum Mach number of the jet (for a $\bar{q}$-ratio matched with full scale) was 0.4. Since this is an unchoked condition, the jet pressure was closely monitored and no significant effects due to nozzle back pressurization were noticed.

On approach, the S/MTD will use both upper and lower vectored jets. In the VRF the vectored jets were simulated using cold compressed air from high-pressure bottles carried on the support vehicle. This limited air supply made it necessary to block the upper ports during this test to minimize the total required mass flow. This is expected to have only a small impact on the ground-effect data, however, because the interaction between the ground plane and vectored thrust flow field is dominated by the lower jets. This will, on the other hand, have an impact on the overall aerodynamics of the configuration. Therefore, the data are presented as increments (instead of total values) in aerodynamic coefficients relative to the out-of-ground-effect values.

It is also essential that the Strouhal number be matched when trying to measure the dynamic effects on a subscale model and relate those to the full-scale condition. To achieve this match,

$$\lambda_M \frac{b_M}{V_M} = \lambda_{\mathrm{FS}} \frac{b_{\mathrm{FS}}}{V_{\mathrm{FS}}}$$

or

$$\lambda_M = \lambda_{\mathrm{FS}} \frac{b_{\mathrm{FS}} V_M}{b_M V_{\mathrm{FS}}}$$

where λ_{FS} represents a frequency of an unsteady characteristic in the flow field to which the full-scale aircraft would respond and λ_M represents that frequency at the model scale. If λ_{FS} is set to be the maximum frequency to which the full-scale aircraft can respond, all frequencies above the resulting λ_M can be filtered from the dynamic data without losing information about how the full-scale aircraft would respond. This is particularly useful in the VRF testing in which the model is driven through the test section and is, therefore, subject to large high-frequency vibrations. The subsequent balance loads (those at frequencies greater than λ_M) can be filtered without removing the unsteady effects that would influence the full-scale aircraft. With the following fixed full-scale values

$\lambda_{\mathrm{FS}} = 3$ Hz
$b_{\mathrm{FS}} = 40$ ft
$V_{\mathrm{FS}} = 197$ ft/sec on approach

(as indicated by the manufacturer) and knowing the model scale to be 0.083, λ_M is a function of the test velocity for a particular run. The data acquired were digitally filtered according to the above discussion.

Procedures

Vectored Thrust

Different thrust vector angles were simulated by attaching different nozzles to the plenum of the thrust simulator. Prior to testing with a particular nozzle, jet-exit total pressures in the center of each nozzle were calibrated against total-pressure measurements taken inside the plenum. After a correlation relationship was established, the total-pressure probes were removed from the nozzle exits and total pressures were computed from the measurements in the plenum chamber. As indicated in table I, the

thrust vector angles tested in the approach configuration were different from those tested in the rollout configuration.

Model Balancing

Because of the nature of the testing in the VRF, large inertial loads are contained in the balance output. In order to remove these loads, the model accelerations must be measured in all six components of motion. Once combined with the mass and moments of inertia of the model, the resulting inertial loads can be subtracted from the balance data. (See the appendix.) This technique can be greatly simplified by balancing the model along all three axes such that the model center of gravity is driven to the point in the model at which the balance center would be located during the test. This was accomplished in several steps. Once the proposed location of the balance moment center was identified in the model, the accelerometers were mounted in the model in such a way as to accurately measure all six components of acceleration of that point. A steel block, which closely resembled the size and weight of only that portion of the balance on the model side of the strain gauge beams of the balance, was then mounted in the model. The model was then suspended from the proposed location of the balance moment center, and weights were added to the inside of the fuselage until the model was balanced at that point along all three axes.

The model was then weighed to determine its mass, a quantity required for inertial load removal. Because the inertial load equations were simplified to an uncoupled system (as outlined in the appendix) by the balancing described above, the moments of inertia could be measured directly through the data acquisition system by shaking the model randomly and recording the accelerations and balance loads. When doing this it is necessary that the aerodynamic loads be assumed to be small. The equations needed for these calculations can be found in the appendix.

Test Conditions

The model was tested primarily in two configurations: the approach configuration and the rollout configuration expected following touchdown . These configurations are defined in table I. The approach configuration was tested at 50, 60, and 70 ft/sec to create three simulated rates of descent. The rates of descent simulated from these velocities were 3.49, 4.19, and 4.88 ft/sec, respectively. All tests of the rollout configuration were conducted at a velocity of 60 ft/sec.

Test Procedure

The vehicle and model were started from rest at one end of the facility and accelerated to the test velocity within 900 ft. The vehicle then passed over the enclosed test section while the model suspended below the vehicle passed through the enclosed test section isolated from the downwash of the vehicle. (See fig. 2.) The test section is approximately 500 ft in length. As the model entered the test section, the model air system was automatically activated and the thrust simulator was powered. This allowed the jets to stabilize before the model passed over the ground board. As the model exited the test section, brakes were applied automatically and stopped the vehicle in less than 100 ft.

Results

Data are presented for two configurations: approach and rollout. The approach configuration is presented first for three rates of descent varying from 3.49 to 4.88 ft/sec while maintaining a $\bar{q}$-ratio of 45. The data for the rollout configuration are then presented. In table I note the differences between these configurations in both the control surface settings and the thrust vector setting. Of principal interest in the data obtained in the approach configuration are the results obtained over the inclined portion of the ground board corresponding to the approach phase of landing (i.e., $h/b > 0.19$). Of principal interest in the rollout configuration data are the measurements taken over the horizontal portion of the ground board ($h/b = 0.19$) and indicated by the solid symbols on the plots.

For both configurations the top thrust-vectoring ports were blocked during this investigation because of a limitation in the air supply capacity. As a result, the aerodynamic coefficients measured are not expected to be the same as those experienced by the S/MTD aircraft during landing. However, it is expected that the increments in the aerodynamic coefficients due to ground effect are valid and useful numbers, since the ground effects associated with the top jets should be small in comparison with those associated with the lower jets. For this reason, the data are presented as increments from the out-of-ground-effect values of lift, pitching moment, and drag coefficients as functions of ground height. The out-of-ground effect values were obtained at $h/b > 3.0$; however, since no change in aerodynamics was seen that far above the ground board, the data are plotted only out to $h/b = 1.5$.

Approach Configuration

For the approach condition, the S/MTD aircraft is trimmed at $\alpha = 12°$, $\delta_h = 1.88°$, $\delta_c = -12.85°$,

and $\delta_a = \delta_f = 20°$ with the upper and lower vectored jets deflected symmetrically up to a deflection angle of 75°, as can be determined from the results found in reference 10. In addition, the upper vectored jet can be deflected an additional 10° if additional thrust control is required; however, the lower jet will not be deflected beyond 75°. The nominal approach thrust vector setting is expected to be 64.3°. This condition, trimmed at $\alpha = 12°$, is noted on a representative lift curve for the F-15 S/MTD in sketch A taken from reference 10. The approach lift coefficient is seen to be approximately 1.1. In this investigation, lower jet vector angles $\delta_{j,l}$ of 45°, 60°, and 80° were tested at three rates of descent, and $\delta_{j,l} = 110°$ was tested at a rate of descent of 4.19 ft/sec.

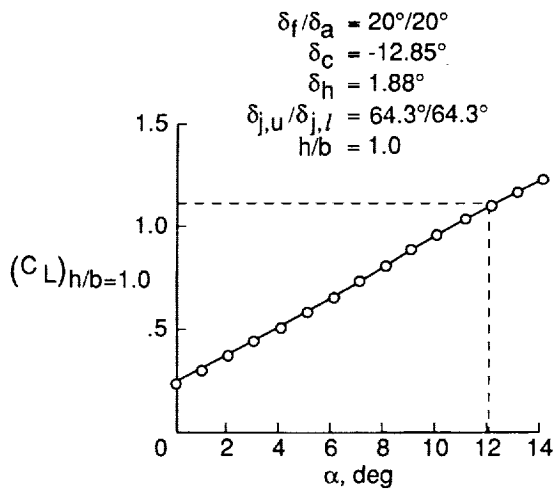

Sketch A

Figures 7–9 contain the increments from the out-of-ground-effect values of the longitudinal coefficients as a function of model height for various rates of descent. Each plot contains three curved lines and three solid symbols. The curved lines represent the dynamic measurements of ground effect over the inclined portion of the ground board at three rates of descent. The solid symbols represent the steady-state measurements of ground effect at minimum ground height over the horizontal portion of the ground board. In general, these measurements show that over the small range of rates of descent tested, there were no significant, consistent differences in the ground effects measured at any of the thrust vector angles. The fact that the small variation in rate of descent did not generate a substantial difference in longitudinal aerodynamics does not imply that there were no effects due to rate of descent but that the effects were relatively constant over the range tested.

Because the effects were so consistent over the range tested, only the data for a rate of descent $\dot{h}$ of 4.2 ft/sec are cross plotted for variations in the lower jet vector angle. This rate of descent was chosen for two reasons: $\delta_{j,l} = 110°$ was tested only at that rate of descent and the rollout configuration data were all obtained at 60 ft/sec—the forward speed used in simulating $\dot{h} = 4.2$ ft/sec.

The effect of the vector angle of the lower jets on the longitudinal aerodynamic coefficients is seen in figure 10. For the lift coefficient at all jet angles tested, the level increased slightly above the out-of-ground-effect level beginning at about $h/b = 1.0$ and remained relatively constant as the model descended to a height of about $h/b = 0.5$ where the lift began to increase sharply. The reason for this two-stage increase is unclear.

For jet vector angles of 45° and 60° (measured from the body axis aft horizontal), the ground effect on the lift coefficient increment was essentially the same; the lift coefficient increased by about 0.24 by minimum ground height. For $\delta_{j,l} = 80°$, the increment in lift coefficient was consistently higher at ground heights below $h/b = 1.0$ than was seen for $\delta_{j,l} = 45°$ and 60°. This is true to an even greater extent at a reverser angle of 110°. Both of these higher thrust vector angles are beyond the range of those intended to be tested by the S/MTD aircraft on approach. At $\delta_{j,l} = 110°$, unlike the results at the other thrust vector angles, the maximum lift coefficient increase occurred before the model was at the wheel touchdown height. At approximately $h/b = 0.22$, the lift coefficient increment reached a maximum value of 0.23 and then dropped to 0.21 by the touchdown height, $h/b = 0.19$. Once at this minimum height, the lift continued to drop (as it transitioned to a steady-state situation) to a level that was actually slightly below the lift level out of ground effect. Often, aircraft are flown such that the sink rate is arrested near the ground. This is referred to as "flaring" the aircraft. These results indicate that such a maneuver could actually allow a lift loss to develop on this configuration, and instead of reducing the rate of descent, flaring would actually cause it to increase. As a consequence, the thrust reverser position of 110° could be used only if an approach procedure were adopted in which the rate of descent was not arrested near the ground.

The effect of the vector angle of the lower jet on the pitching moment is presented in figure 10(b). For all thrust vector angles, as the model moved closer to the ground board and the horizontal stabilizer moved into ground effect, the lift on that surface increased as indicated by the nose-down pitching-moment increment. At higher thrust vector angles ($\delta_{j,l} = 80°$ and 110°), a ground vortex is able to develop under the horizontal stabilizer and the low pressure associated

with a ground vortex induces an incremental nose-up pitching moment. An explanation of the ground vortex and its development can be found in reference 11.

For the three vector angles that span the angles expected to be flight tested (45°, 60°, and 80°), the pitching-moment coefficient continued to decrease down to the minimum ground height. The magnitude of this negative pitching-moment increment increased slightly as the jets were vectored farther forward from $\delta_{j,l} = 45°$ to $\delta_{j,l} = 80°$. When the jets were vectored to $\delta_{j,l} = 110°$, the ground effect was somewhat different. From $h/b = 0.5$ down to $h/b = 0.28$, consistent with the other vector angles, pitching moment decreased; however, the magnitude of this decrease was slightly greater than that for the other vector angles. At $h/b = 0.28$, though, the pitching moment began to increase. The pitching moment returned to its free-stream level by $h/b = 0.25$, continued to increase to $\Delta C_m = 0.18$ by touchdown height, and then increased more to $\Delta C_m = 0.20$ over the horizontal portion of the ground board.

The ground effect of the jet vector angle on the drag coefficient can be seen in figure 10(c). As was the case with lift and pitching-moment coefficients, no ground effects were seen above about $h/b = 1.0$. At that height the drag coefficient increased slightly and remained relatively constant as the model descended to a height of about $h/b = 0.5$ where the drag began to increase rapidly.

For the three vector angles that span the expected flight-approach thrust vector range, there was a steady increase in drag coefficient to a ΔC_D level of about 0.04 at the minimum height. In general, this increase is consistent with the increase in lift seen above. When the jets were vectored to $\delta_{j,l} = 110°$, the drag increase in ground effect was larger than that for the aft vectored cases for all heights between $h/b = 1.0$ and $h/b = 0.3$. Below $h/b = 0.3$, the drag increment steadily decreased down to the minimum height where the drag coefficient returned to nearly the free-stream level. Once at touchdown height ($h/b = 0.19$), the drag coefficient continued to decrease to a level of $\Delta C_D = -0.055$ below the free-stream level, again indicating that this vector angle would be useful only if an approach procedure were adopted in which the rate of descent was not arrested near the ground.

Rollout Configuration

For the rollout configuration, the data of practical application to the S/MTD program are those obtained over the horizontal portion of the ground board simulating the actual rollout phase of a landing. As a consequence of the technique used, the aerodynamic effect of decreasing h/b was also measured and has, therefore, been included in this paper. These results are presented in figure 11.

For all thrust reverser angles tested ($\delta_{j,l} = 90°$, 120°, and 135°), the lift coefficient began to increase near $h/b = 0.8$ and continued to do so to the minimum ground height. The magnitude of this increment in lift increased as the reverser jets were vectored farther forward from the 90° position. Once over the horizontal portion of the ground board, the flow fields of all three thrust reverser configurations continued to change significantly. The solid symbols on the plots indicate the steady-state level of the lift coefficient increment at that minimum height.

Perhaps more meaningful is a plot of the effect of power on the steady-state increment in the lift coefficient. This is plotted in figure 12(a). Because the thrust loads are not carried through the balance, this plot shows the induced effects at wheel touchdown height of the various thrust reverser angles. For all angles tested there is a significant lift increase in comparison with the unpowered case.

At heights greater than the wheel touchdown height of $h/b = 0.19$, all three thrust reverser angles induced slight nose-down pitching moments below $h/b = 0.4$ as can be seen in figure 11(b). In the rollout phase (over the horizontal portion of the ground board), the steady-state increments in pitching moment ΔC_m increased from essentially zero at $\delta_{j,l} = 90°$ to 0.20 at $\delta_{j,l} = 120°$, and finally to 0.31 at $\delta_{j,l} = 135°$.

Again, a more meaningful illustration of these results is seen when the increments in the pitching moment between the powered and unpowered cases are plotted for the different thrust reverser angles. This can be seen in figure 12(b). The data show that as the jets were vectored farther forward, pitching moment increased. This is probably due to both an increased downwash on the horizontal stabilizer resulting from entrainment and an increased upwash at the canard generated by the presence of a progressively larger ground vortex under the configuration.

With respect to the drag coefficient, in general, there was a slight drag reduction with reducing h/b, but only below $h/b = 0.22$. This is illustrated in figure 11(c). Once at the minimum height, the two forward-blowing cases ($\delta_{j,l} = 120°$ and 135°) showed significant drag reductions in comparison with the out-of-ground-effect drag coefficient for the same configurations. For the case where the jets were blown vertically ($\delta_{j,l} = 90°$), the drag coefficient at minimum ground height was the same as that out of ground effect.

The increment in drag due to power for this configuration is plotted as a function of thrust reverser

vector angle in figure 12(c). These data show increased drag due to increased lift at $\delta_{j,l} = 90°$. It is believed that as the jets were blown farther forward, the increased downwash induced at the horizontal stabilizer and the increased upwash induced at the canard generated the incremental aerodynamic loads shown sketched in figure 13. Because of the orientation of these surfaces in the rollout configuration, these increments reduced the drag on the configuration. Since no flow visualization was available, however, these interpretations are strictly speculative; yet, they do appear to explain the characteristics seen in the aerodynamic data.

Comparison With the Simulation Data Base

The static data used in this comparison were provided by the McDonnell Aircraft Company based on a six-degree-of-freedom interpolation of the wind-tunnel data from reference 12 used in the construction of the simulation data base. There are two major differences between that static wind-tunnel test (the procedure described in ref. 12) and the moving-model test performed at the VRF. First, the VRF data were obtained while simulating a rate of descent. Second, the wind-tunnel measurements were made in the presence of a ground boundary layer that has been shown to have a significant impact on the development of the ground vortex created by vectored jets near a ground board. This impact is detailed in reference 11. In short, the presence of a ground boundary layer allows the ground vortex to penetrate significantly farther upstream (approximately 30 percent) than would be possible in its absence. These two differences are believed to be the source of the differences between the two data sets discussed below. Other differences considered less significant between the tests are outlined in table III.

It should also be pointed out that the plots presented for the wind-tunnel data at $\delta_{j,l} = 110°$ are based largely on interpolations and, to some extent, extrapolations. For this nozzle design, reversed thrust is not intended to be used on approach. Therefore, the wind-tunnel test of the approach configuration of the S/MTD was not conducted through full height transition with reversed thrust. The thrust vector angle of 110° was tested out of ground effect and at $h/b = 0.35$ in the approach configuration; however, at wheel touchdown height it was tested only in the rollout configuration (i.e., with low angles of attack and low lift configuration). The plots represent the best approximation of the simulation data base based on that information.

To a lesser extent, the other plots are also based on interpolations of the data used in the simulation data base. For example, the wind-tunnel data were obtained at $\delta_{j,l} = 45°$, 65°, 80°, and 110°, whereas the moving-model data were obtained at $\delta_{j,l} = 45°$, 60°, 80°, and 110°. For comparison, the wind-tunnel results at $\delta_{j,l} = 45°$ and 65° were interpolated to $\delta_{j,l} = 60°$.

In figure 14(a), the lift increment in ground effect for the approach configuration has been plotted for $\delta_{j,l} = 45°$ and 60°. As height decreases to touchdown height, the static wind-tunnel data consistently predict a greater lift increment due to ground effect than that predicted by the VRF data set. This difference is attributed to the effects of rate-of-descent modeling in the VRF. Once at the minimum ground height for some time, the results from the VRF tests are seen to have the same steady-state lift-increment levels as those in the wind-tunnel data base.

Figure 14(b) illustrates the effect of vectoring the jets farther forward. The presence of the ground boundary layer is seen to have a greater effect. For both $\delta_{j,l} = 80°$ and $\delta_{j,l} = 110°$, not only is the lift increment different as h/b reduces to the minimum ground height but also the steady-state levels measured once the models were at that minimum height are different. The reason for the differences at the minimum ground height is believed to be due to the presence of a ground boundary layer in the wind-tunnel testing. The differences at the other ground heights are due to both the rate-of-descent modeling in the VRF and the presence of a ground boundary layer in the wind-tunnel testing—these two effects cannot be separated for this particular set of data.

The differences in pitching moment are similarly illustrated in figure 15. At $\delta_{j,l} = 45°$, much like the results seen for the lift coefficient, the wind-tunnel data base predicts a greater nose-down pitching moment than the dynamic measurements from the VRF as the model height is reduced to the minimum ground height. However, once the model was at that minimum height for some time and the VRF flow field transitioned to a steady state, the levels of nose-down pitching moment measured by the two test techniques are nearly equal. Again, this difference at heights greater than that corresponding to wheel touchdown is attributed to the modeling of a rate of descent in the VRF testing.

As the jets were vectored further to $\delta_{j,l} = 60°$, the comparison is similar down to a model height of approximately $h/b = 0.3$. Below that height the wind-tunnel data base indicates that the configuration experienced progressively less nose-down pitching moment as the model approached the ground. This is, again, believed to be due to the presence of the ground boundary layer in the wind-tunnel testing. This boundary layer allows the vectored jets

to penetrate farther upstream along the wall before forming the ground vortex. In this situation it is believed that the ground vortex has developed under the horizontal stabilizer and the low-pressure vortex has reduced the lift on that surface. Greater penetration of the ground vortex should also induce greater upwash at the wing. The net effect would be as shown in figures 14 and 15: increased steady-state pitching-moment increment and no difference in lift increment between the VRF data and the wind-tunnel data base.

The effect of the ground boundary layer is even more pronounced as the jets are vectored farther forward. In these configurations, more upwash is indicated at the canard in the wind-tunnel data base than was indicated in the VRF results because the ground vortex could not penetrate as far upstream in the absence of a ground boundary layer.

Similar results were found in the drag measurements as shown in figure 16. Again, at $\delta_{j,l} = 45°$, where the jets are blown well aft, the presence of the ground boundary layer in the wind-tunnel test had little effect on the steady-state aerodynamics, but as the thrust was directed progressively farther forward, the boundary-layer effect was intensified as was seen in both lift and pitching moment. For all settings, a significant effect is evident because of rate-of-descent modeling in the VRF at all model heights greater than the minimum height.

Concluding Remarks

A moving-model ground-effect testing method has been used to study the influence of rate of descent on the aerodynamics of the F-15 STOL and Maneuver Technology Demonstrator (S/MTD) configuration for both the approach and rollout phases of landing. The approach phase was modeled for three rates of descent, and over the small range of rates of descent tested, no significant differences could be seen in the results. However, a comparison of the rate-of-descent results with predictions from the F-15 S/MTD simulation data base (predictions based on data obtained in a wind tunnel with zero rate of descent) showed significant differences due both to the rate of descent in the moving-model test and to the presence of the ground boundary layer in the static wind-tunnel test. Relative to the simulation data base predictions, the rate-of-descent modeling produced substantially less lift increase in ground effect, less nose-down pitching moment, and less increase in drag. These differences became more prominent at the larger thrust vector angles.

The differences between the static and dynamic ground-effect measurements are significant, and it appears that the dynamic technique more accurately represents aircraft approach conditions. This implies a need for dynamic ground-effect testing on future configurations that utilize vectored thrust on approach.

The results of this investigation indicate no safety-of-flight problems with the lower jets vectored up to 80° on approach. The results also indicate that this configuration could employ a nozzle concept using lower jet vector angles up to 110° on approach if a "no-flare" approach procedure were adopted and if inlet reingestion does not pose a problem.

NASA Langley Research Center
Hampton, VA 23665-5225
April 24, 1990

Acknowledgment

The author would like to thank Garrett Billman of the McDonnell Douglas Corporation for providing the predictions on the aerodynamic characteristics of the F-15 S/MTD used for comparison in this report. These predictions were made based on the simulation data base.

Appendix

Special Corrections

In most steady-state wind-tunnel tests it is assumed that

$$\sum_{i=1}^{n} k\frac{\Delta x_i}{n} = F_{\text{aero}}$$

(assuming small interactions between channels) where k is the balance sensitivity constant, Δx is the one-dimensional balance deflection, F_{aero} is the aerodynamic force in the x-direction, and n is the number of samples averaged for each point. The data are averaged to remove high-frequency variations between points, some of which are caused by vibrations of the model. In dynamic testing, however, averaging of samples is not desired because meaningful high-frequency information can be lost. Making dynamic force and moment measurements on a moving model presents a unique problem because the driving system imposes additional vibrational loads on the model that can mask the meaningful measurements.

In this investigation, the system of the model, balance, and support system was treated as a spring-mass-damper system and the various loads measured by the balance were computed in an effort to remove the unwanted vibratory loads from the meaningful data. Following is a derivation of the type of equation used. In this demonstration, the equation will be derived for one degree of freedom only—in this case, the axial direction on the model.

According to Newton's second law of motion for a one-dimensional spring-mass-damper system on a fixed base in a vacuum,

$$m\ddot{x}_M + c\dot{x}_M + kx_M = 0$$

In this equation, m is the mass of everything on the model side of the strain gauges of the balance (the spring), c is the internal damping of the balance, and k is the spring constant of the balance. The subscript M denotes the motions of the mass on the model side of the balance. If the base of the system is allowed to move, the equation becomes

$$m\ddot{x}_M + c\dot{x}_M - c\dot{x}_B + kx_M - kx_B = 0$$

The subscript B refers to motions of the base of the system. These equations can be found in reference 13. If the system is then placed in a homogeneous atmosphere, an aerodynamic damping term is also included. For this one-dimensional study of the axial motion of the model, this damping force is known to be of the form of the aerodynamic axial force defined as $C_A\frac{\rho S}{2}\dot{x}^2$ so that the equation becomes

$$C_A\frac{\rho S}{2}\dot{x}_M^2 + m\ddot{x}_M + c\,\Delta\dot{x} + k\,\Delta x = 0$$

If the flow field is then permitted to have an unsteady component (in this case due to the effect of upwash as the model enters ground effect and the effects of thrust reversers near the ground), this will also be represented as an aerodynamic damping term. The equation then takes the form

$$C_A\frac{\rho S}{2}\left(\dot{x}_M^2 + \dot{x}_{\text{FF}}^2\right) + m\ddot{x}_M + c\,\Delta\dot{x} + k\,\Delta x = 0$$

Let $C'_A = -C_A\frac{\rho S}{2}$, and then separate $\dot{x}_M$ into a steady component $\dot{x}_{M,\text{SS}}$ and an unsteady component $\dot{x}_{M,\text{osc}}$. This latter component represents the component of the velocity generated by the model vibrations and results in unwanted aerodynamic loads that contaminate the

balance output. The term $\dot{x}_{M,\mathrm{ss}}$ represents the steady-state forward velocity of the model and is, on the other hand, meaningful. With these changes the equation becomes

$$C'_A\left(\dot{x}^2_{M,\mathrm{SS}} + \dot{x}^2_{\mathrm{FF}}\right) = k\,\Delta x + c\,\Delta\dot{x} + m\ddot{x}_M - C'_A\dot{x}^2_{M,\mathrm{osc}}$$

The term $C'_A\dot{x}^2_{M,\mathrm{osc}}$ is very difficult to approximate because C_A is most likely not constant with time on an oscillating model. Reference 14 shows that because of viscosity, aerodynamic effects require a finite amount of time to achieve a steady-state level. That is, in fact, the very premise for the need for this test technique. Because of the inability to solve for this component, no attempt was made to remove it from the results mathematically. The term $\ddot{x}_M$, however, was measured and the inertial term $m\ddot{x}_M$ can be removed from the data. If it is assumed that the balance damping is small with respect to the inertial term and that the term $C'_A\dot{x}^2_{M,\mathrm{osc}}$ will be faired by hand from the resultant aerodynamic loads, the equation becomes

$$F_{\mathrm{aero}} = k\,\Delta x + m\ddot{x}_M$$

This is the form of the equation for a one-dimensional system. When this is expanded into six degrees of freedom (and F_{aero} in the axial direction is replaced by F_{AF}), the matrix becomes

$$\begin{bmatrix} F_{\mathrm{NF}} \\ F_{\mathrm{AF}} \\ F_{\mathrm{PM}} \\ F_{\mathrm{RM}} \\ F_{\mathrm{YM}} \\ F_{\mathrm{SF}} \end{bmatrix} = \begin{bmatrix} \mathrm{NF} \\ \mathrm{AF} \\ \mathrm{PM} \\ \mathrm{RM} \\ \mathrm{YM} \\ \mathrm{SF} \end{bmatrix} + \begin{bmatrix} -m & 0 & -m\bar{x} & m\bar{y} & 0 & 0 \\ 0 & m & m\bar{z} & 0 & m\bar{y} & 0 \\ -m\bar{x} & -m\bar{z} & -I_Y & 0 & 0 & 0 \\ -m\bar{y} & 0 & 0 & -I_X & 0 & -m\bar{z} \\ 0 & m\bar{y} & 0 & 0 & I_Z & m\bar{x} \\ 0 & 0 & 0 & m\bar{z} & m\bar{x} & m \end{bmatrix} \begin{bmatrix} \ddot{z} \\ \ddot{x} \\ \dot{q} \\ \dot{p} \\ \dot{r} \\ \ddot{y} \end{bmatrix}$$

Clearly, this can be greatly simplified if the model center of gravity is driven to the moment center of the balance (i.e., if $\bar{x} = \bar{y} = \bar{z} = 0$). If done, the equations simplify to the linear system

$$\begin{aligned} F_{\mathrm{NF}} &= \mathrm{NF} - m\ddot{z} \\ F_{\mathrm{AF}} &= \mathrm{AF} + m\ddot{x} \\ F_{\mathrm{PM}} &= \mathrm{PM} - I_Y\dot{q} \\ F_{\mathrm{RM}} &= \mathrm{RM} - I_X\dot{p} \\ F_{\mathrm{YM}} &= \mathrm{YM} + I_Z\dot{r} \\ F_{\mathrm{SF}} &= \mathrm{SF} + m\ddot{y} \end{aligned}$$

This is the form of the equations used in the data analysis. In this form the moments of inertia I_X, I_Y, and I_Z could be measured directly through the data acquisition system by shaking the model randomly and recording the accelerations and balance loads. If the aerodynamic loads are assumed to be small, each moment of inertia is the relationship between a particular balance output and a particular accelerometer output.

As mentioned earlier, an aerodynamic damping term still remains in the resultant forces and moments, and therefore it is necessary to remove this by hand fairing the data. Also uncertain is the effect of $\dot{x}_{M,\mathrm{osc}}$ on $\dot{x}_{\mathrm{FF}}$. That is, how does the oscillating model influence the development of the ground-effect flow field? The present investigation did not answer this question.

References

1. Schade, Robert O.: *Ground Interference Effects.* NASA TN D-727, 1961.
2. Thomas, James L.; Hassell, James L., Jr.; and Nguyen, Luat T.: Aerodynamic Characteristics in Ground Proximity. *Powered-Lift Aerodynamics and Acoustics,* NASA SP-406, 1976, pp. 145–158.
3. Kotansky, D. R.; and Glaze, L. W.: STOL Landing Thrust–Reverser Jet Flowfields. *Proceedings of the 1985 NASA Ames Research Center's Ground-Effects Workshop,* Kerry Mitchell, ed., NASA CP-2462, 1987, pp. 289–308.
4. Kemmerly, Guy T.; and Paulson, John W., Jr.: *Investigation of a Moving-Model Technique for Measuring Ground Effects.* NASA TM-4080, 1989.
5. Roberts, Franklin D.: The F-15 STOL and Maneuver Technology Demonstrator (S/MTD) Program. *Proceedings of the International Powered Lift Conference,* P-203, Soc. of Automotive Engineers, Inc., 1988, pp. 705–714. (Available as SAE Paper 872383.)
6. Satran, Dale R.; Neuhart, Dan; Holbrook, G. Thomas; and Greene, George C.: Vortex Research Facility Improvements and Preliminary Density Stratification Effects on Vortex Wakes. AIAA-85-0050, Jan. 1985.
7. Maskew, Brian: Prediction of Subsonic Aerodynamic Characteristics: A Case for Low-Order Panel Methods. *J. Aircr.,* vol. 19, no. 2, Feb. 1982, pp. 157–163.
8. Joshi, P. B.: *Generic Thrust Reverser Technology for Near Term Application. Volume 1. Background and Program Overview.* AFWAL-TR-84-3094-VOL. I, U.S. Air Force, Feb. 1985. (Available from DTIC as AD B094 292L.)
9. Schwantes, E.: *The Recirculation Flow Field of a VTOL Lifting Engine.* NASA TT F-14,912, 1973.
10. Kemmerly, Guy T.: A Comparison of the Ground Effects Measured With and Without Rate-of-Descent Modeling on the F-15 S/MTD Configuration. AIAA-89-3280-CP, Aug. 1989.
11. Stewart, V. R.; and Kemmerly, G. T.: Characteristics of the Ground Vortex Formed by a Jet Moving Over a Fixed Ground Plane. AIAA-89-0650, Jan. 1989.
12. McDonnell Douglas Corp.: *STOL and Maneuver Technology Demonstrator (S/MTD) Program.* WRDC-TR-89-3050, *Volume II,* U.S. Air Force, May 1989. (Available from DTIC as AD B133 240.)
13. Gainer, Thomas G.; and Hoffman, Sherwood: *Summary of Transformation Equations and Equations of Motion Used in Free-Flight and Wind-Tunnel Data Reduction and Analysis.* NASA SP-3070, 1972.
14. Ericsson, L. E.; and Reding, J. P.: Fluid Mechanics of Dynamic Stall, Part I. Unsteady Flow Concepts. *J. Fluids & Struct.,* vol. 2, no. 1, Jan. 1988, pp. 1–33.

Table I. Definition of Test Configurations

Configuration	α, deg	δ_f/δ_a, deg	δ_c, deg	δ_h, deg	δ_j, deg
Approach	12	20/20	−13	2	45
	12	20/20	−13	2	60
	12	20/20	−13	2	80
	12	20/20	−13	2	110
Rollout	0	0/0	−10	10	90
	0	0/0	−10	10	120
	0	0/0	−10	10	135

Table II. Roll Deviations From Horizontal of Principal Surfaces

Aerodynamic surface	Roll angle from horizontal, deg
Canard	0.40
Wing	−0.08
Horizontal stabilizer	−0.38

Table III. Minor Differences in Testing Conditions Between the Wind Tunnel and the VRF

Variable	Wind tunnel	VRF
Model scale	7.5 percent	8.3 percent
Test Mach number	0.18	0.05
Landing gear	On	Off
Canopy type	Two seat	Single seat

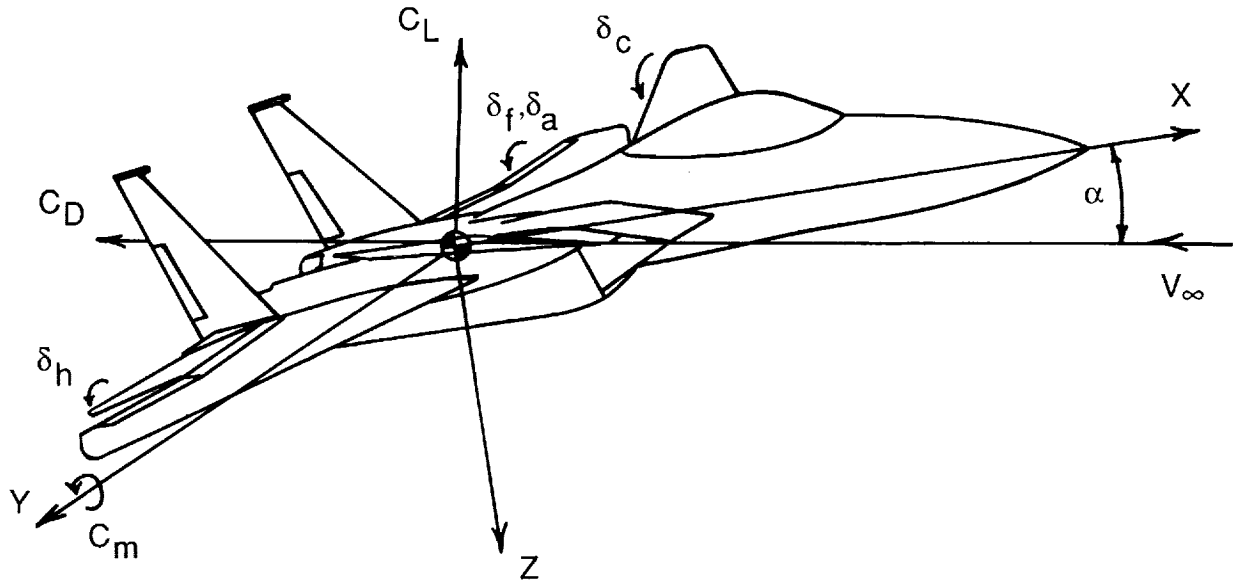

Figure 1. Coordinate system used for presentation of results.

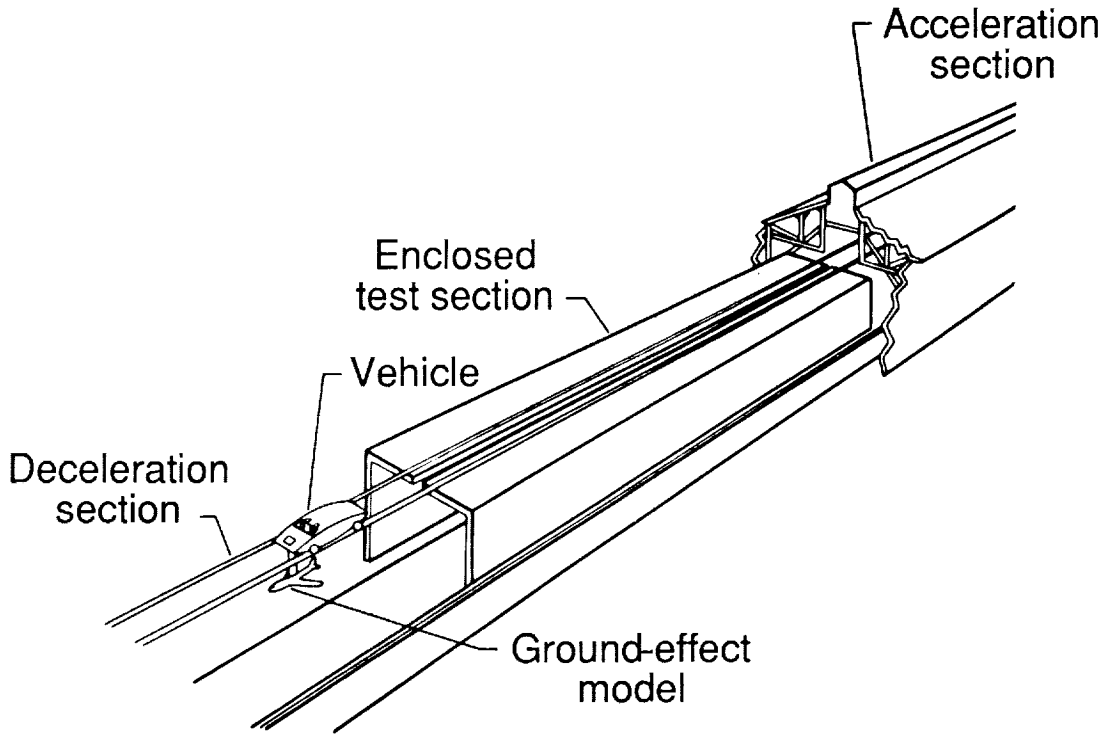

Figure 2. Schematic diagram of the VRF.

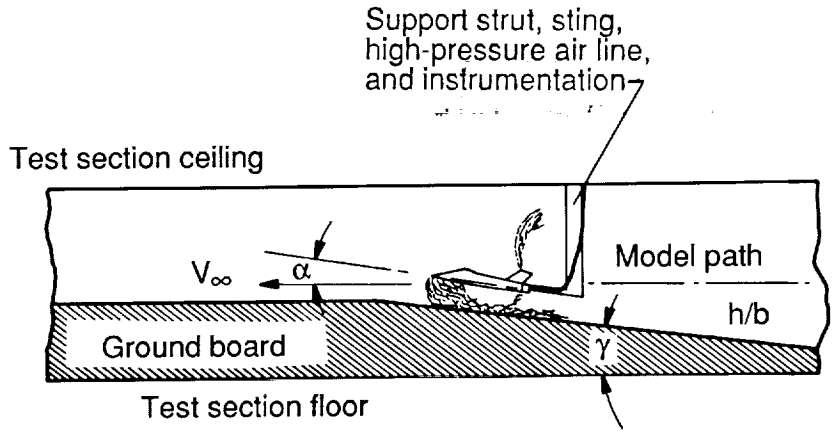

Figure 3. Model passing through test section in the VRF.

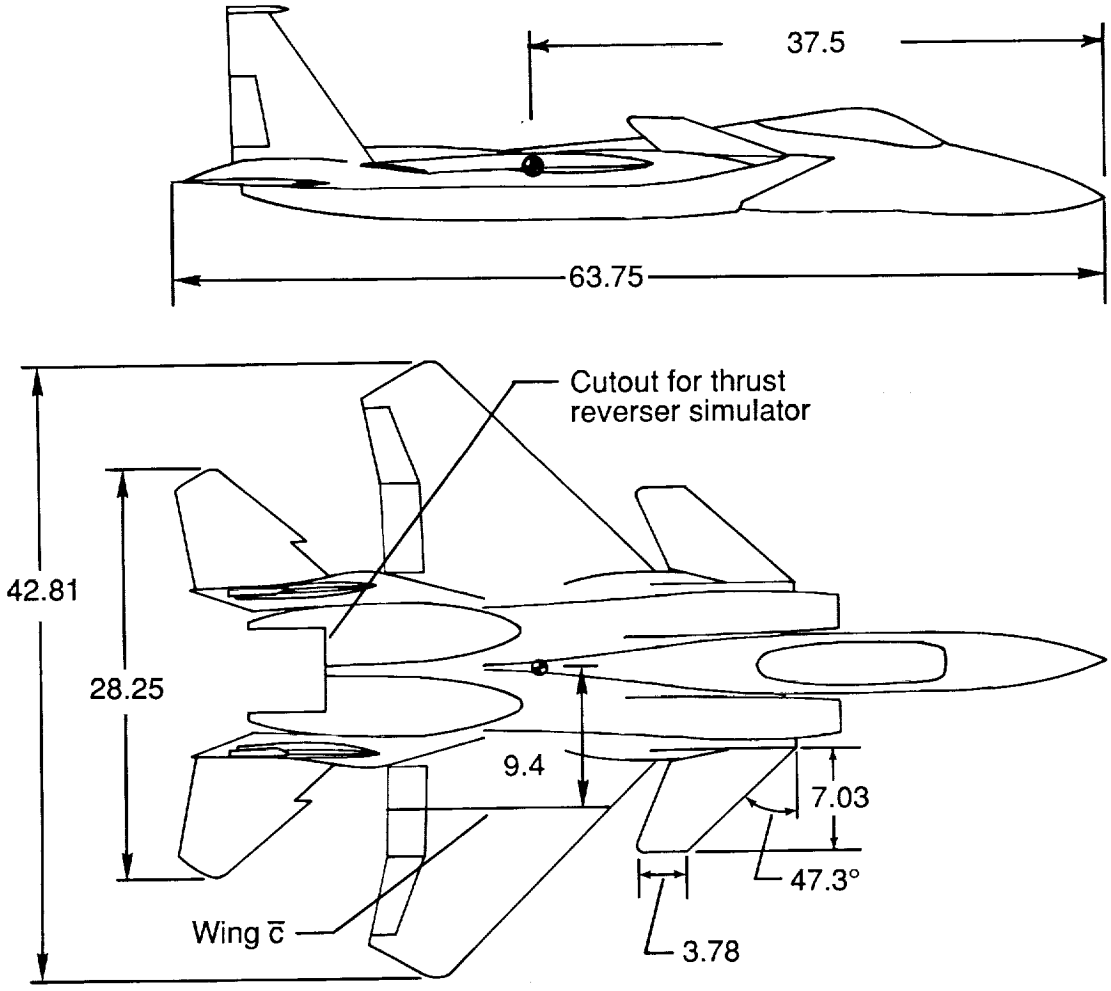

Figure 4. Sketch of the F-15 S/MTD model. Linear dimensions are given in inches.

L-88-2598

Figure 5. The F-15 S/MTD model mounted in the VRF.

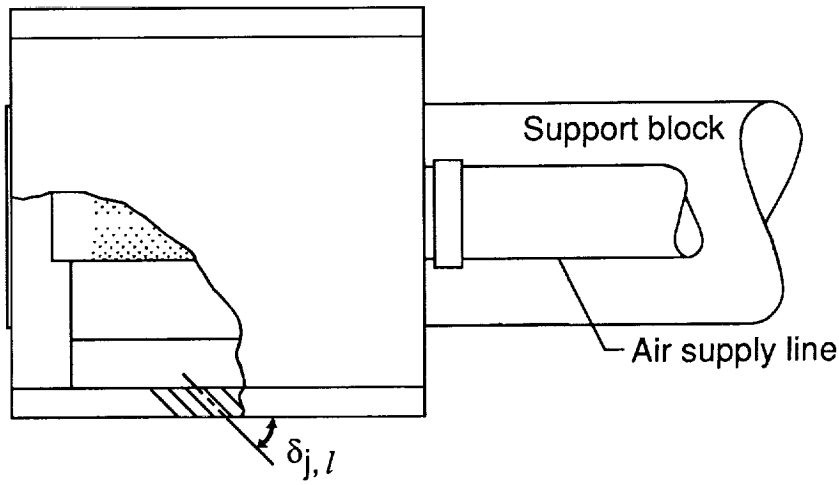

(a) Side view.

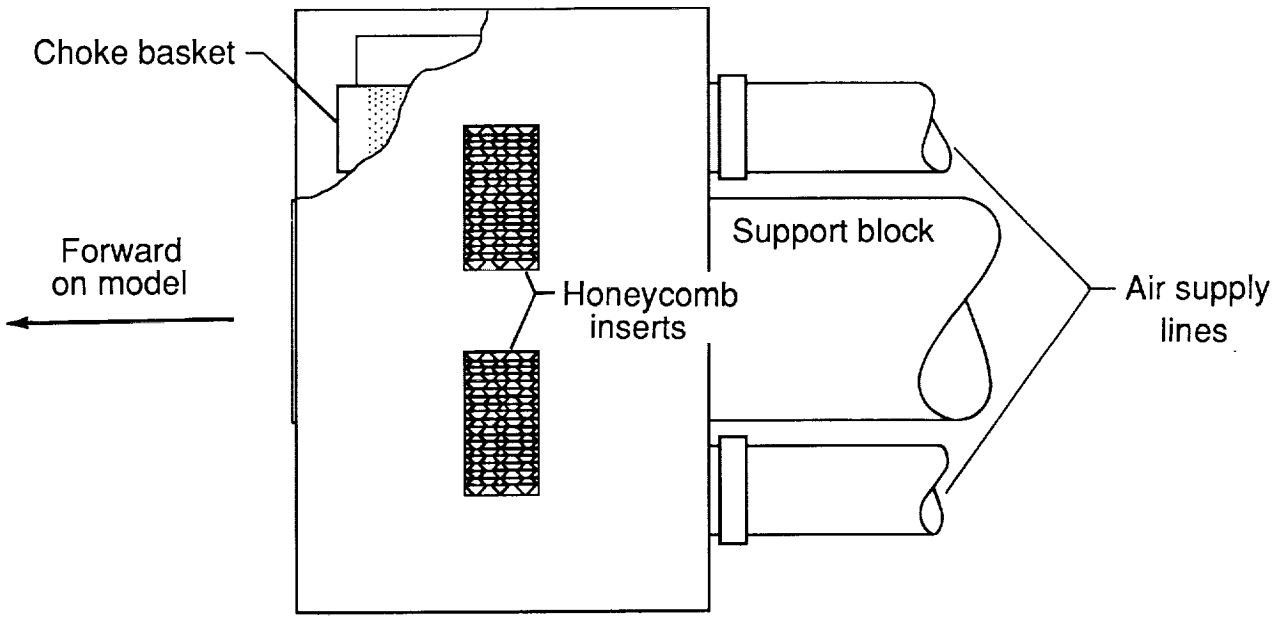

(b) Bottom view.

Figure 6. Sketch of vectored thrust simulator.

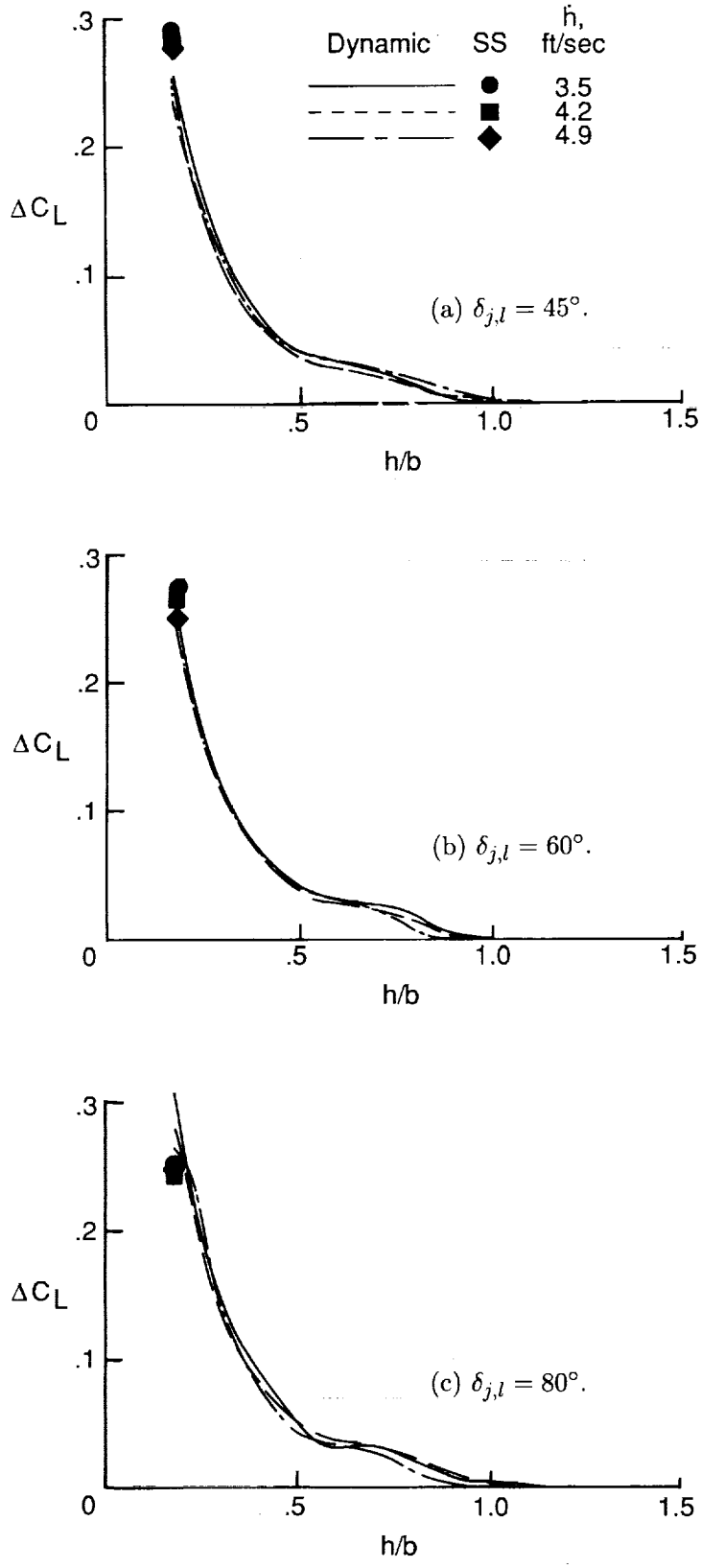

Figure 7. Effect of model height on incremental lift coefficient of the S/MTD approach configuration at three rates of descent. $\alpha = 12°$; $\delta_f/\delta_a = 20°/20°$; $\delta_c = -13°$; $\delta_h = 2°$.

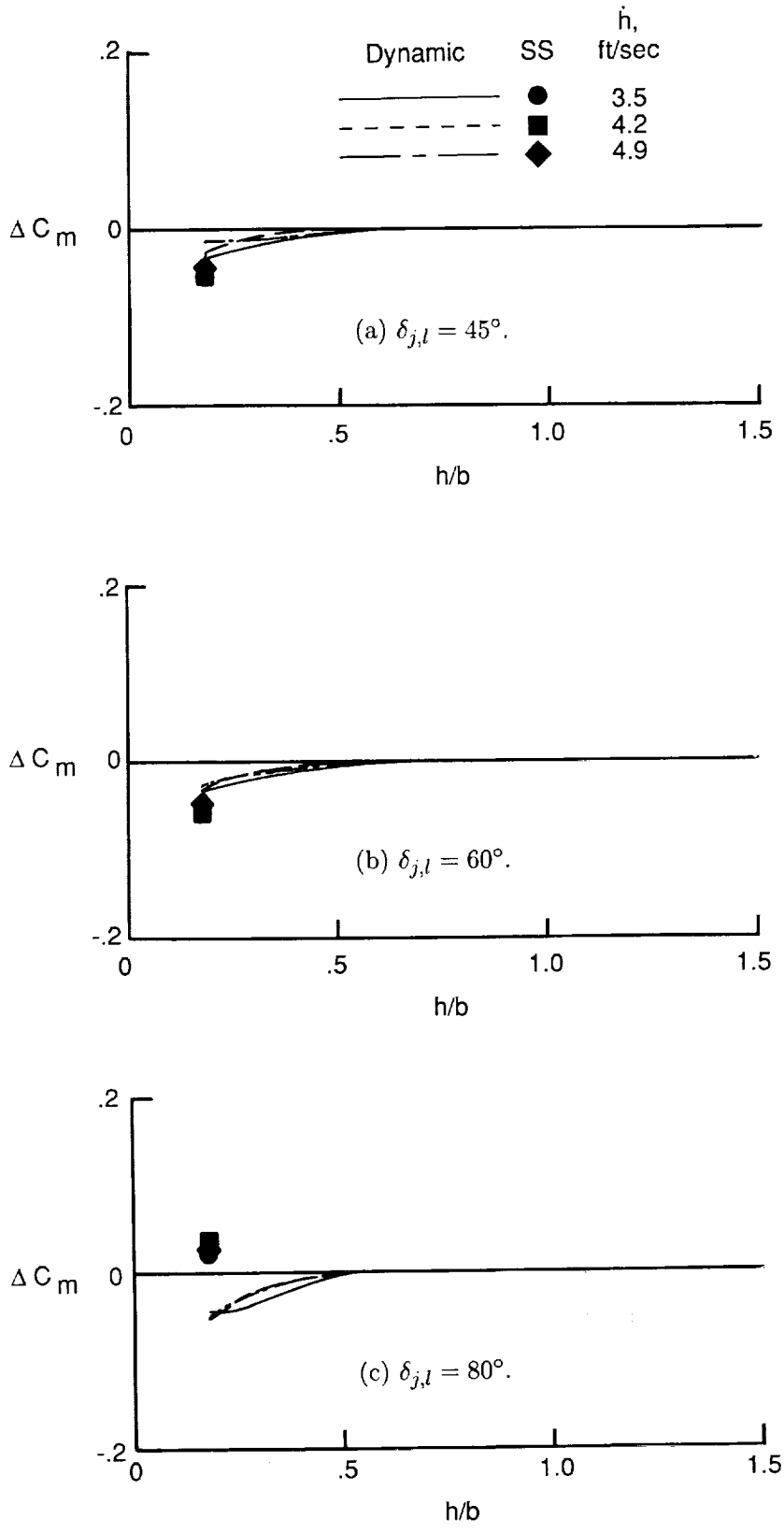

Figure 8. Effect of model height on incremental pitching-moment coefficient of the S/MTD approach configuration at three rates of descent. $\alpha = 12°$; $\delta_f/\delta_a = 20°/20°$; $\delta_c = -13°$; $\delta_h = 2°$.

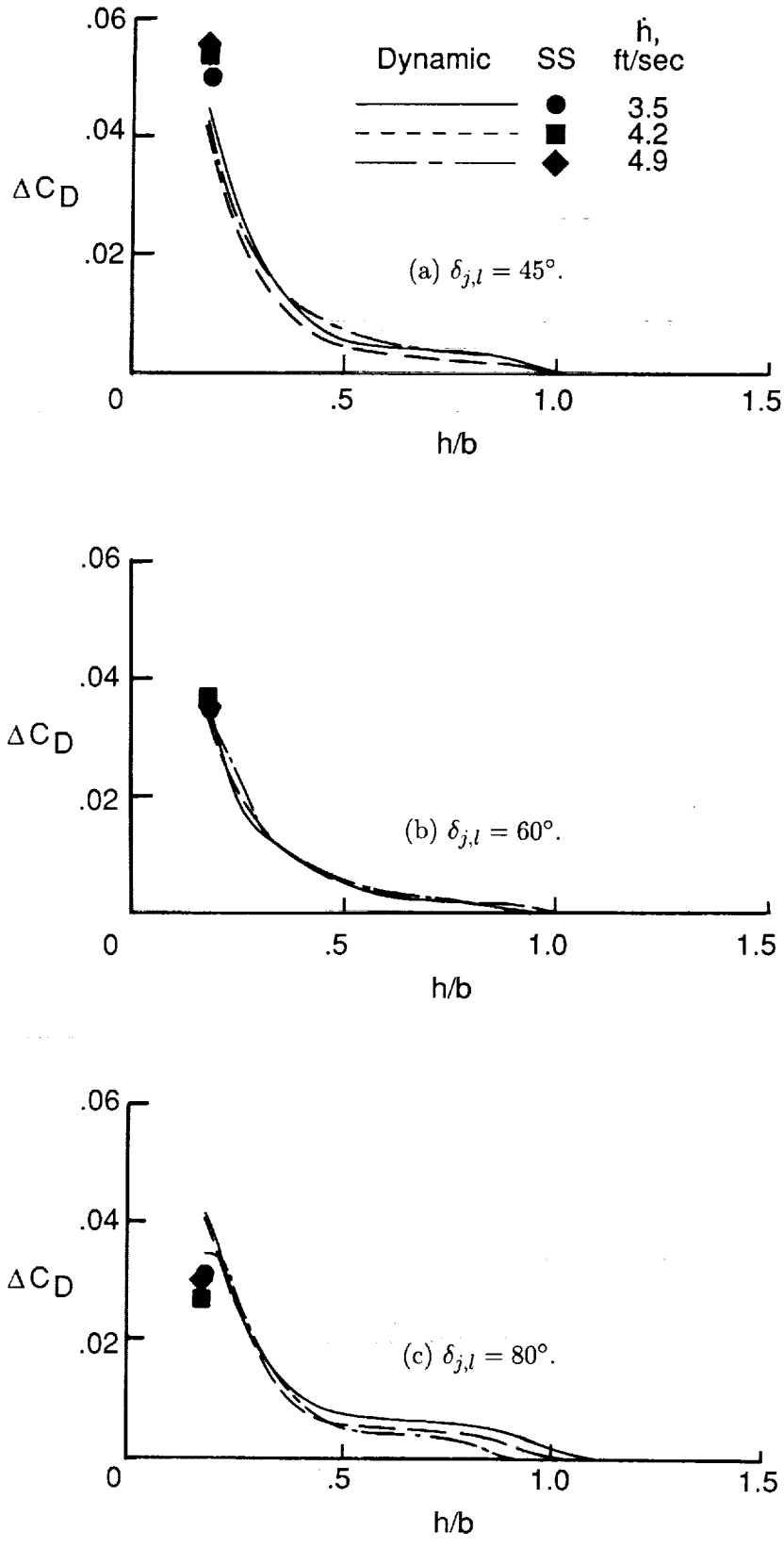

Figure 9. Effect of model height on incremental drag coefficient of the S/MTD approach configuration at three rates of descent. $\alpha = 12°$; $\delta_f/\delta_a = 20°/20°$; $\delta_c = -13°$; $\delta_h = 2°$.

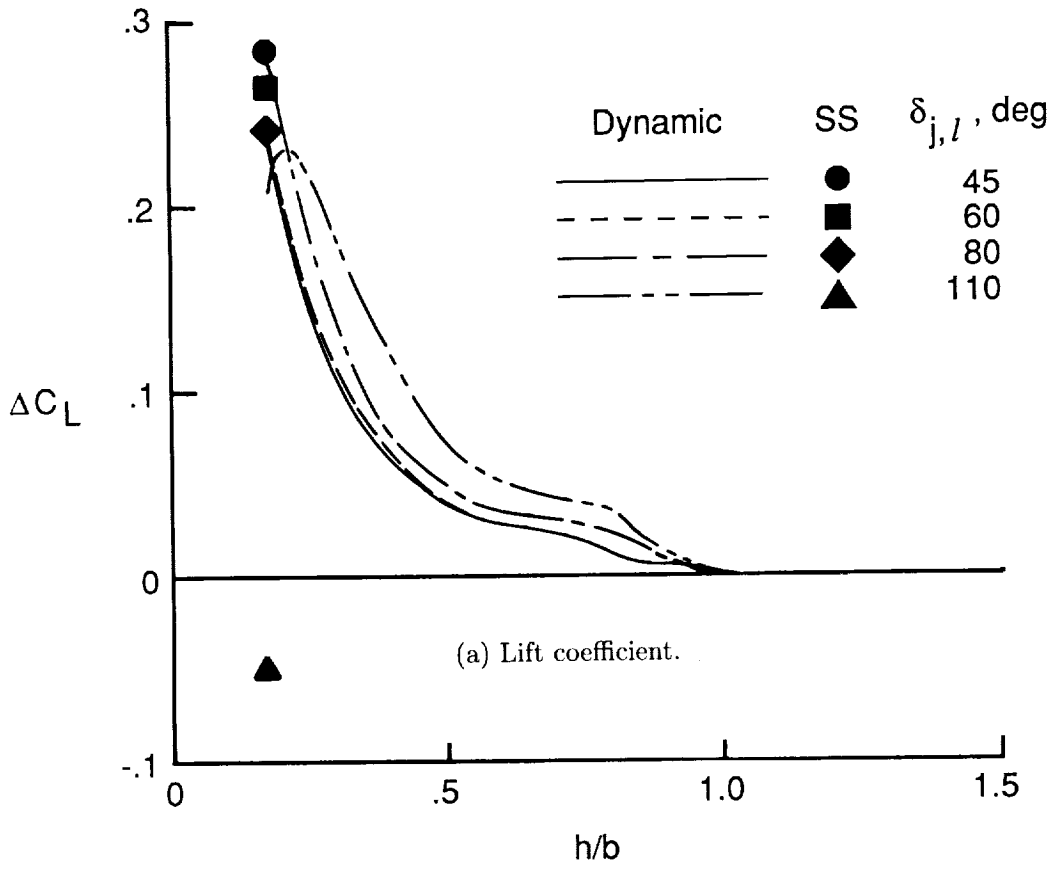

(a) Lift coefficient.

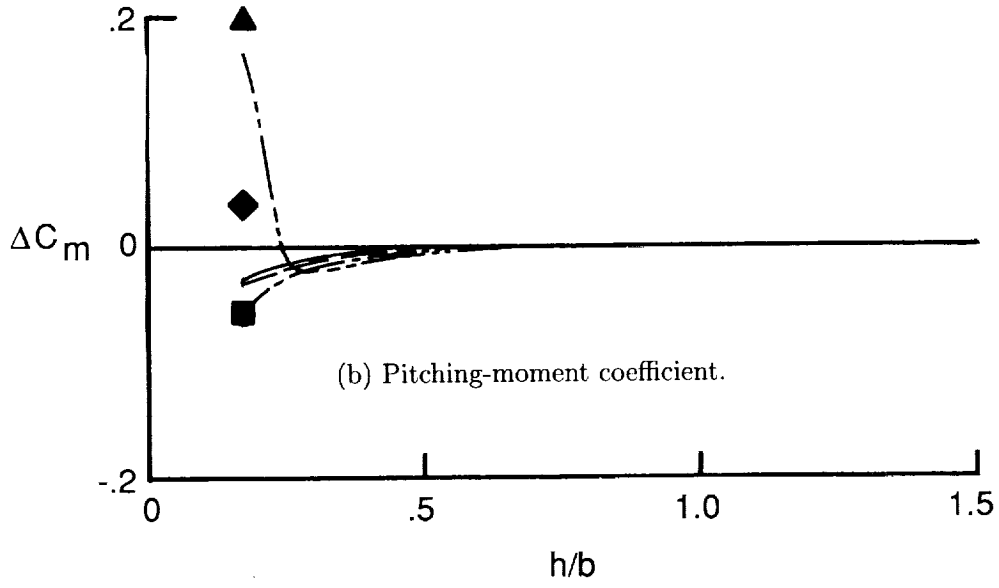

(b) Pitching-moment coefficient.

Figure 10. Effect of model height on longitudinal aerodynamics of the S/MTD approach configuration at four thrust reverser vector angles. $\alpha = 12°$; $\delta_f/\delta_a = 20°/20°$; $\delta_c = -13°$; $\delta_h = 2°$.

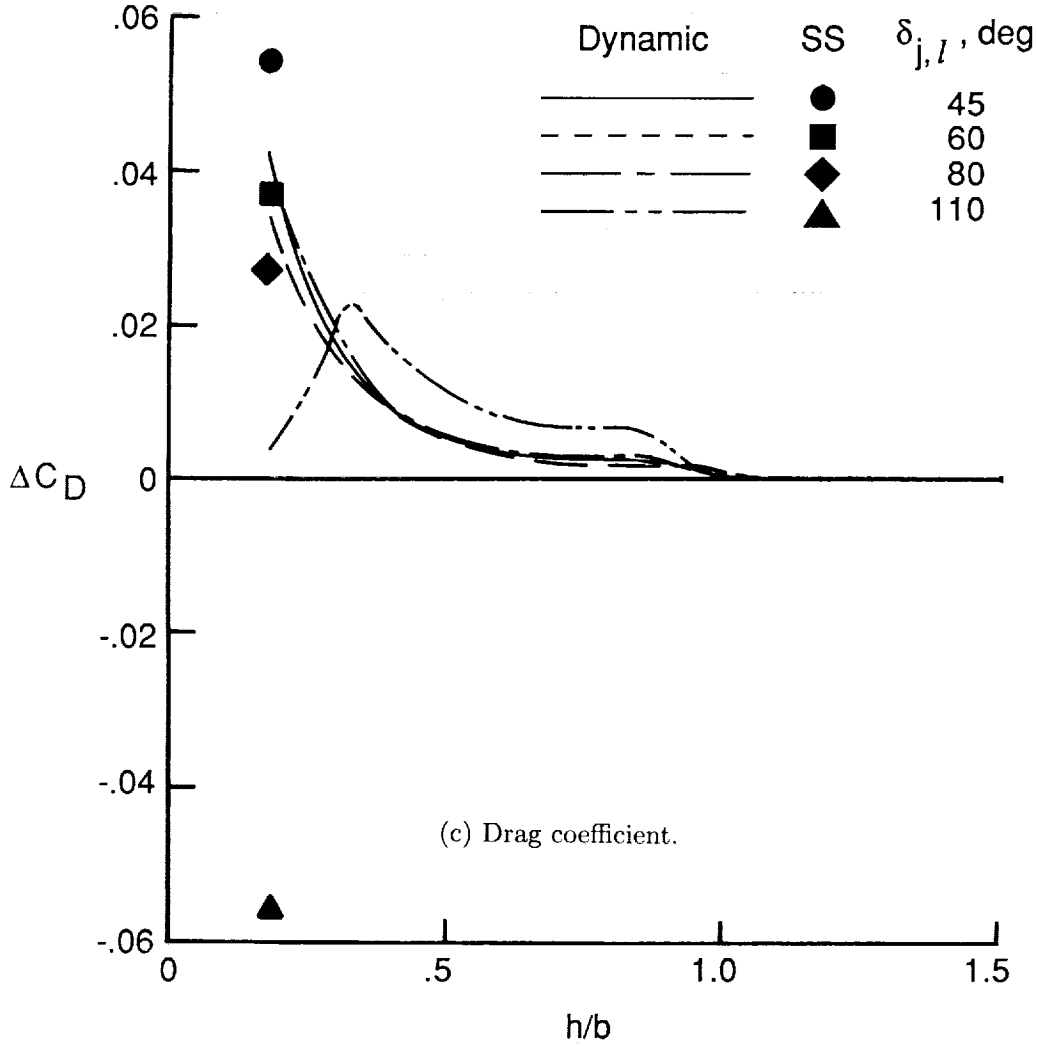

(c) Drag coefficient.

Figure 10. Concluded.

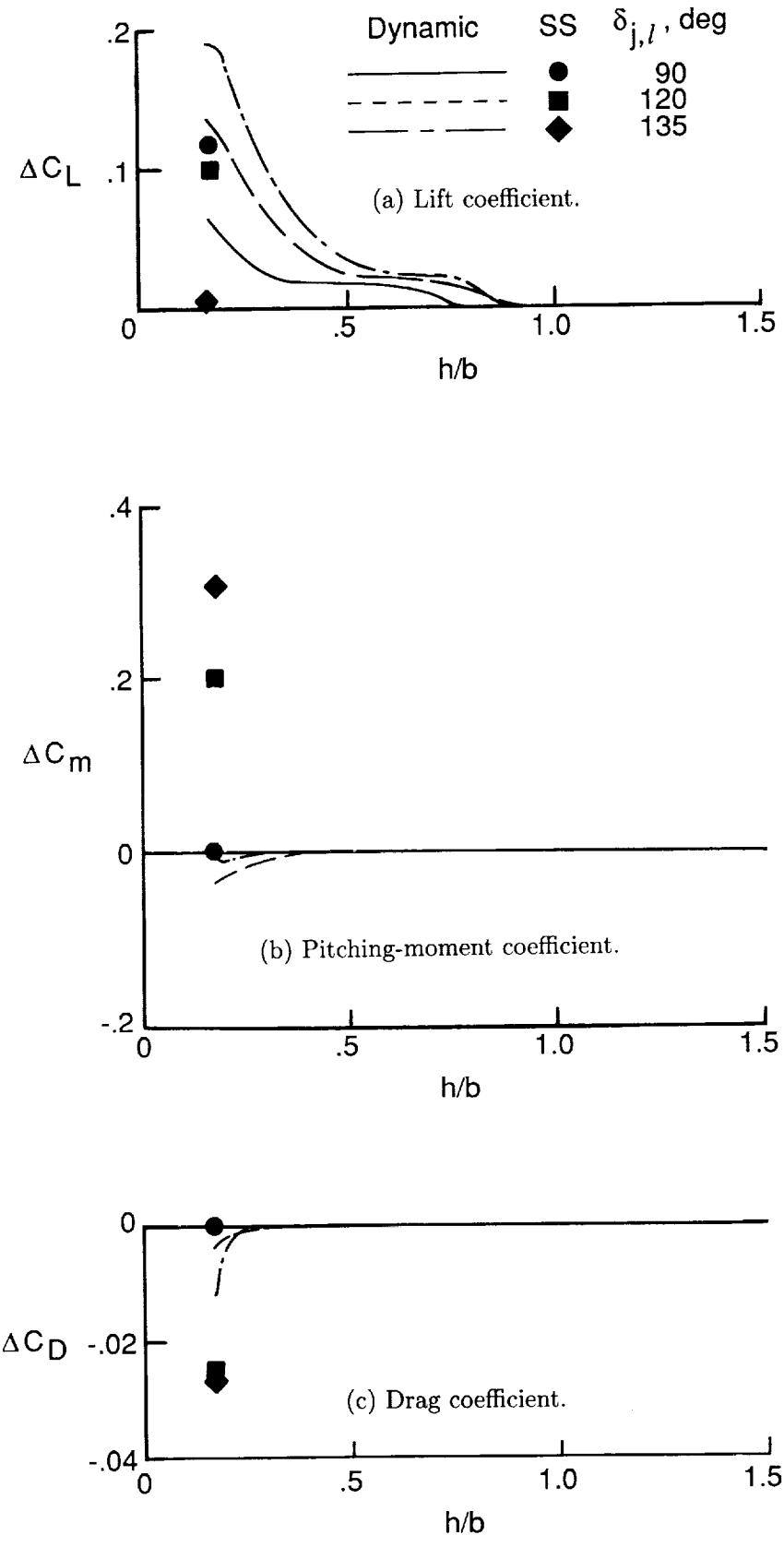

Figure 11. Effect of model height on longitudinal aerodynamics of the S/MTD rollout configuration at three thrust reverser vector angles. $\alpha = 0°$; $\delta_f/\delta_a = 0°/0°$; $\delta_c = -10°$; $\delta_h = 10°$.

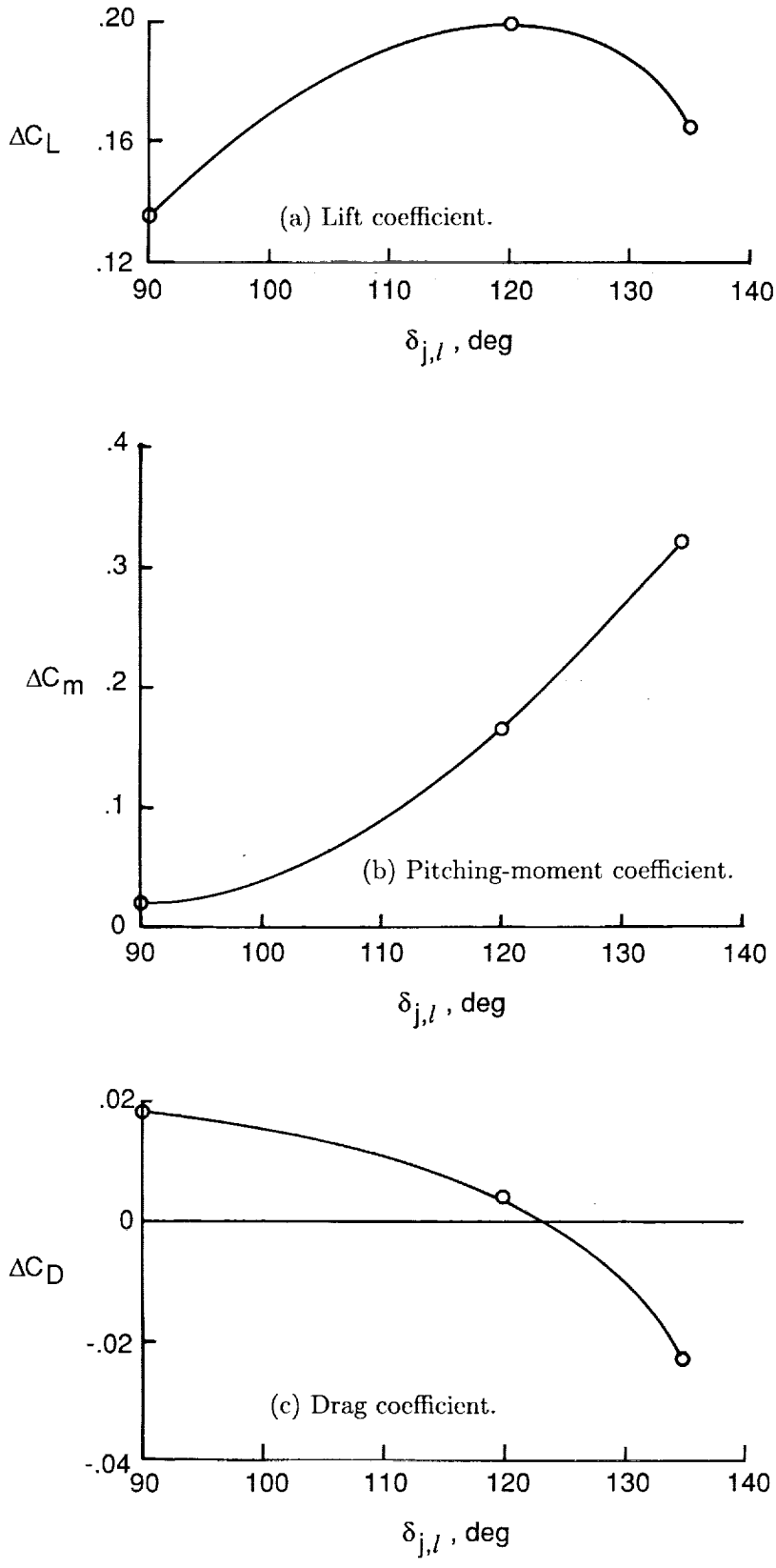

Figure 12. Steady-state effect on longitudinal aerodynamics of operating thrust reverser at wheel touchdown height in rollout configuration. $\alpha = 0°$; $\delta_f/\delta_a = 0°/0°$; $\delta_c = -10°$; $\delta_h = 10°$.

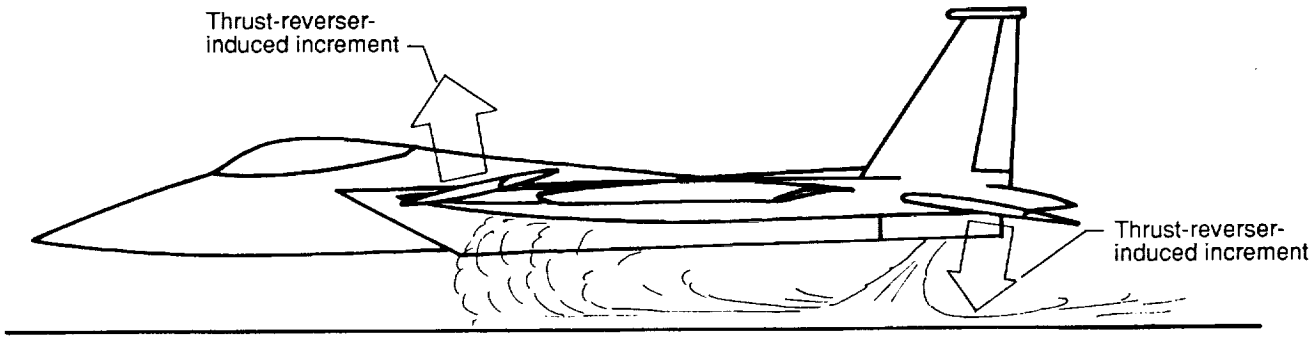

Figure 13. Incremental loads generated on canard and horizontal stabilizer due to thrust reverser operation at wheel touchdown height in rollout configuration. $\alpha = 0°$; $\delta_f/\delta_a = 0°/0°$; $\delta_c = -10°$; $\delta_h = 10°$.

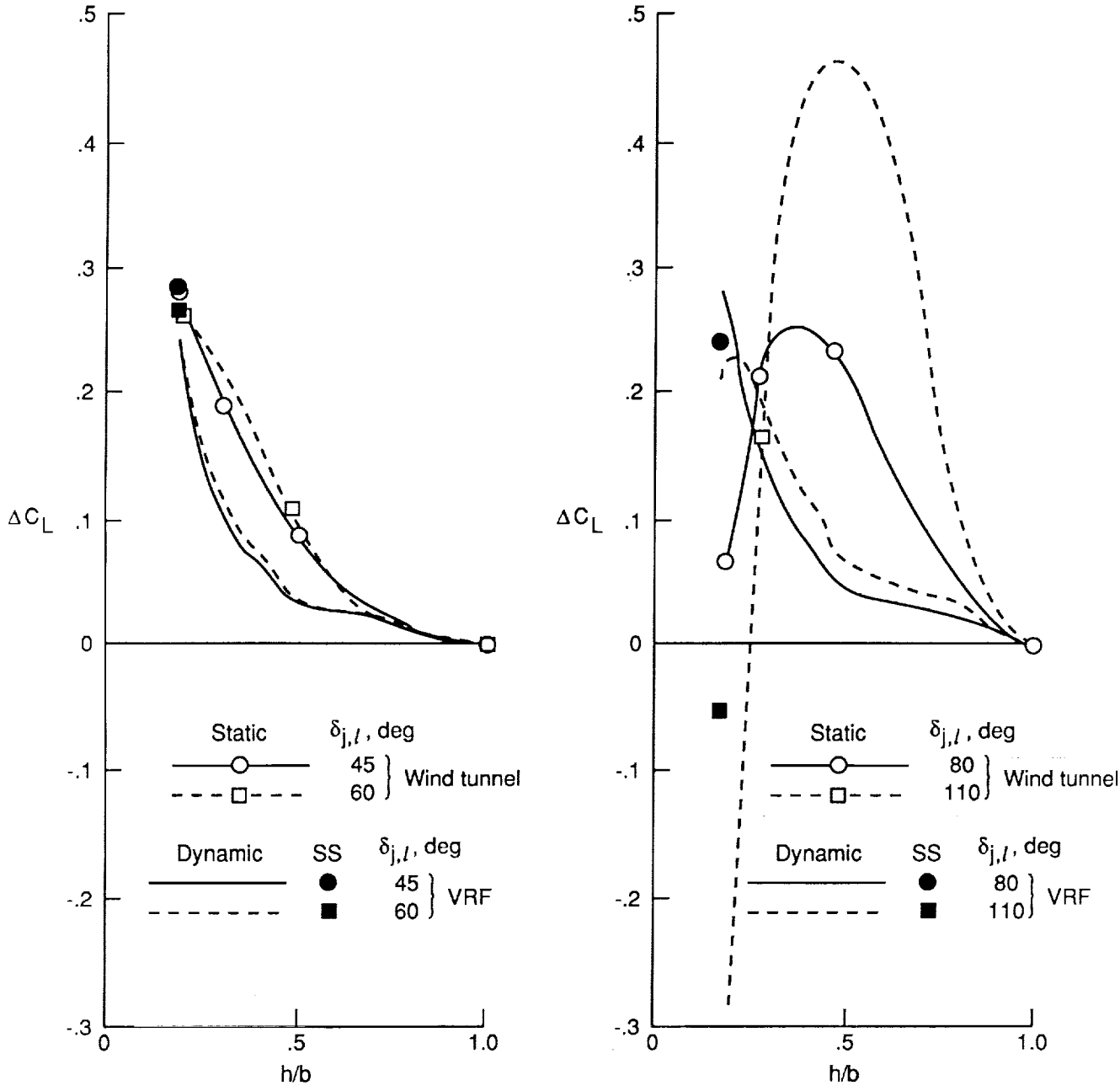

(a) $\delta_{j,l} = 45°$ and $60°$.

(b) $\delta_{j,l} = 80°$ and $110°$.

Figure 14. Comparison of static and dynamic ground effects on lift coefficient of the F-15 S/MTD approach configuration. $\alpha = 12°$; $\delta_f/\delta_a = 20°/20°$; $\delta_c = -13°$; $\delta_h = 2°$.

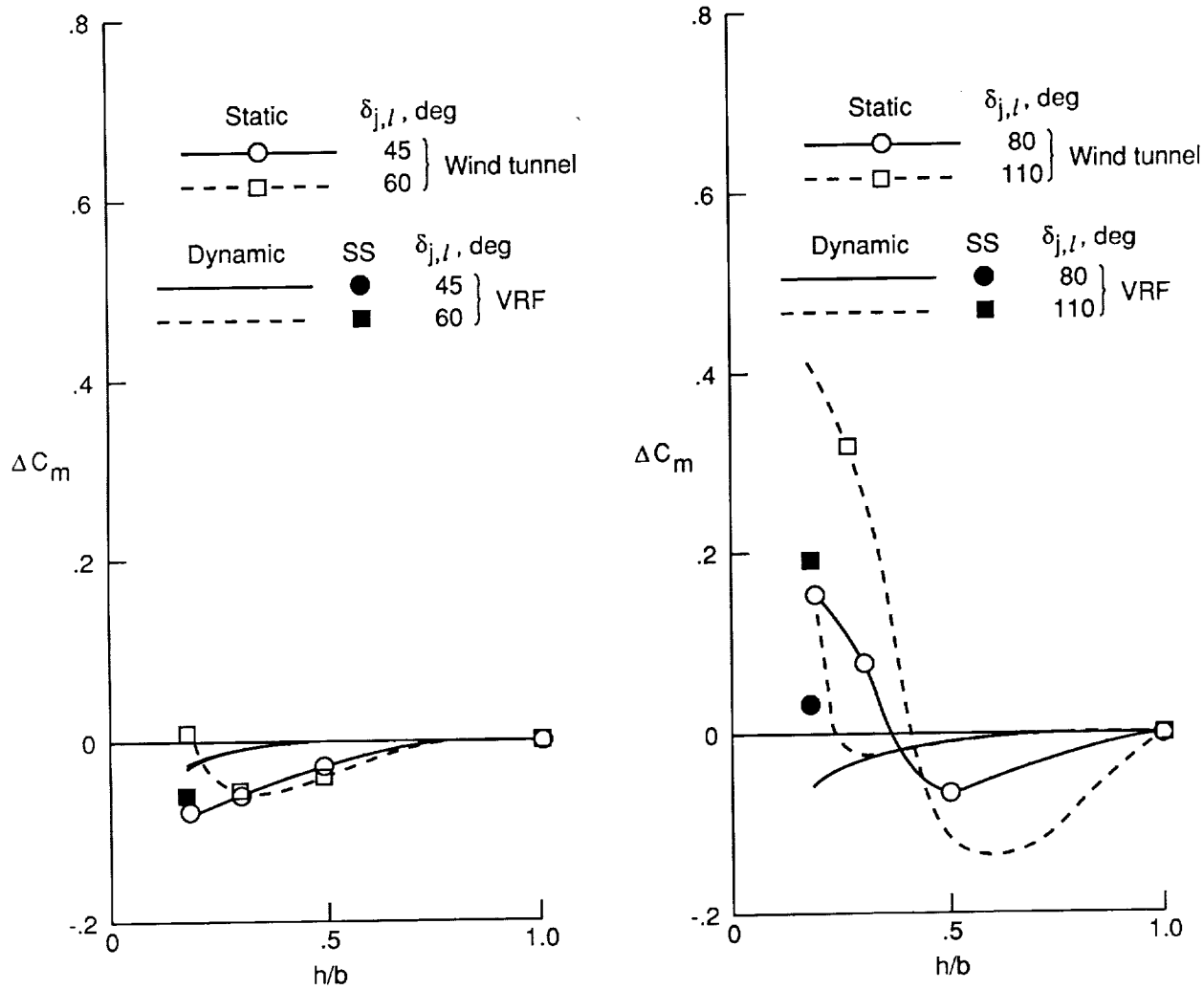

(a) $\delta_{j,l} = 45°$ and $60°$.

(b) $\delta_{j,l} = 80°$ and $110°$.

Figure 15. Comparison of static and dynamic ground effects on pitching-moment coefficient of the F-15 S/MTD approach configuration. $\alpha = 12°$; $\delta_f/\delta_a = 20°/20°$; $\delta_c = -13°$; $\delta_h = 2°$.

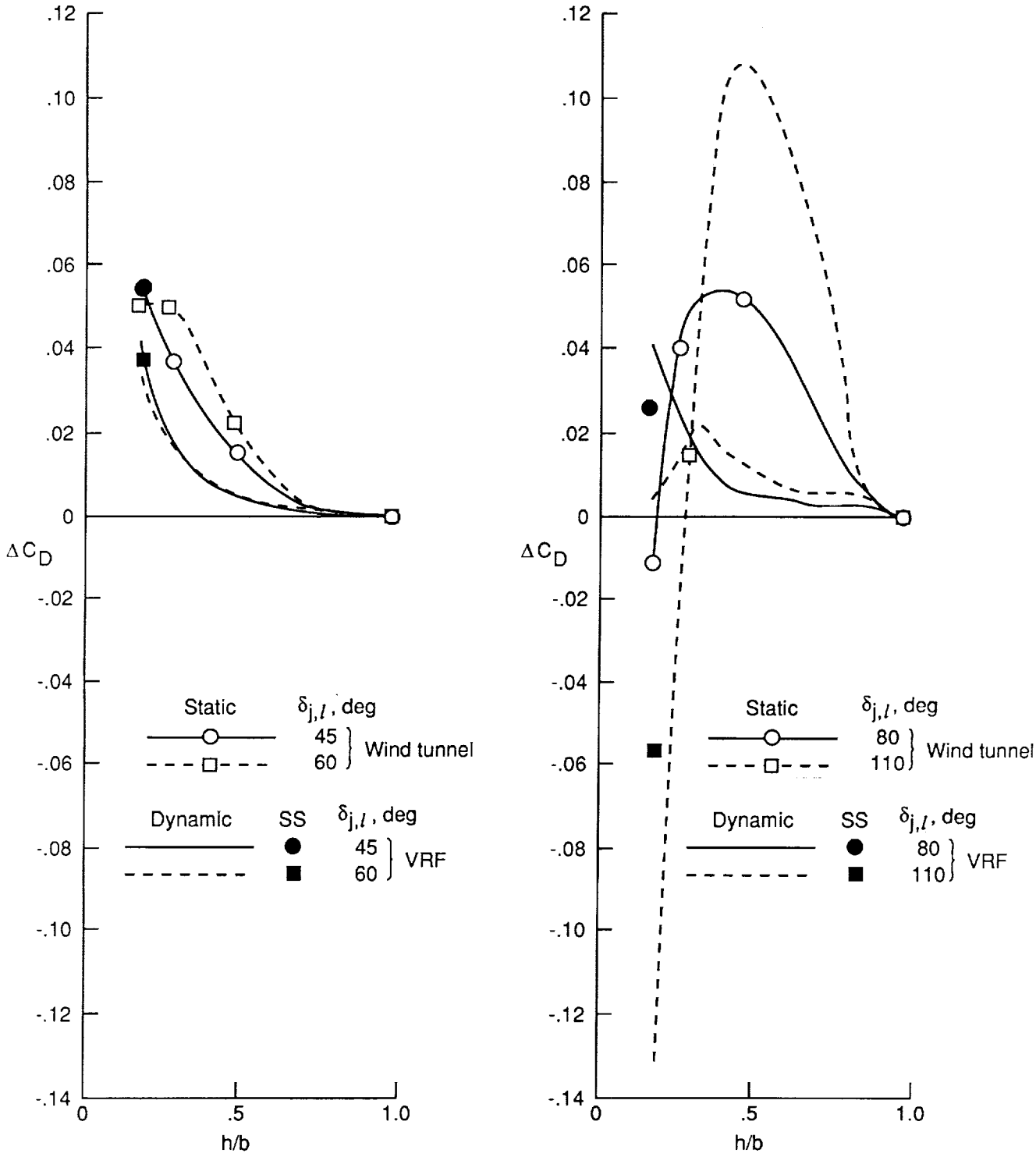

(a) $\delta_{j,l} = 45°$ and $60°$.

(b) $\delta_{j,l} = 80°$ and $110°$.

Figure 16. Comparison of static and dynamic ground effects on drag coefficient of the F-15 S/MTD approach configuration. $\alpha = 12°$; $\delta_f/\delta_a = 20°/20°$; $\delta_c = -13°$; $\delta_h = 2°$.

NASA
National Aeronautics and Space Administration

Report Documentation Page

1. Report No.	2. Government Accession No.	3. Recipient's Catalog No.
NASA TP-3000		

4. Title and Subtitle	5. Report Date
Dynamic Ground-Effect Measurements on the F-15 STOL and Maneuver Technology Demonstrator (S/MTD) Configuration	June 1990
	6. Performing Organization Code
7. Author(s)	8. Performing Organization Report No.
Guy T. Kemmerly	L-16555
9. Performing Organization Name and Address	10. Work Unit No.
NASA Langley Research Center Hampton, VA 23665-5225	505-61-71-02
	11. Contract or Grant No.
12. Sponsoring Agency Name and Address	13. Type of Report and Period Covered
National Aeronautics and Space Administration Washington, DC 20546-0001	Technical Paper
	14. Sponsoring Agency Code

15. Supplementary Notes

16. Abstract

A moving-model ground-effect testing method has been used to study the influence of rate of descent on the aerodynamic characteristics of the F-15 STOL and Maneuver Technology Demonstrator (S/MTD) configuration for both the approach and rollout phases of landing. The approach phase was modeled for three rates of descent and the results were compared with predictions from the F-15 S/MTD simulation data base (predictions based on data obtained in a wind tunnel with zero rate of descent). This comparison showed significant differences due both to the rate of descent in the moving-model test and to the presence of the ground boundary layer in the static wind-tunnel test. Relative to the simulation data base predictions, the moving-model test showed substantially less lift increase in ground effect, less nose-down pitching moment, and less increase in drag. These differences became more prominent at the larger thrust vector angles. Over the small range of rates of descent tested using the moving-model technique, the effect of rate of descent on longitudinal aerodynamics was relatively constant. The results of this investigation indicate no safety-of-flight problems with the lower jets vectored up to 80° on approach. The results also indicate that this configuration could employ a nozzle concept using lower reverser vector angles up to 110° on approach if a "no-flare" approach procedure were adopted and if inlet reingestion does not pose a problem.

17. Key Words (Suggested by Authors(s))
Ground effects
S/MTD
Ground testing
Thrust reverser
Dynamic testing

18. Distribution Statement
Unclassified—Unlimited

Subject Category 02

19. Security Classif. (of this report)	20. Security Classif. (of this page)	21. No. of Pages	22. Price
Unclassified	Unclassified	29	A03